

Analysis of adiabatic shear coupled to ductile fracture and melting in viscoplastic metals

J.D. Clayton^{1*}

¹Terminal Effects Division, Army Research Directorate
DEVCOM ARL, Aberdeen, MD 21005-5066, USA

Abstract

Material failure by adiabatic shear is analyzed in viscoplastic metals that can demonstrate up to three distinct softening mechanisms: thermal softening, ductile fracture, and melting. An analytical framework is constructed for studying simple shear deformation with superposed static pressure. A continuum power-law viscoplastic formulation is coupled to a ductile damage model and a solid-liquid phase transition model in a thermodynamically consistent manner. Criteria for localization to a band of infinite shear strain are discussed. An analytical-numerical method for determining the critical average shear strain for localization and commensurate stress decay is devised. Averaged results for a high-strength steel agree reasonably well with experimental dynamic torsion data. Calculations probe possible effects of ductile fracture and melting on shear banding, and vice-versa, including influences of cohesive energy, equilibrium melting temperature, and initial defects. A threshold energy density for localization onset is positively correlated to critical strain and inversely correlated to initial defect severity. Tensile pressure accelerates damage softening and increases defect sensitivity, promoting shear failure. In the present steel, melting is precluded by ductile fracture for loading conditions and material properties within realistic protocols. If heat conduction, fracture, and damage softening are artificially suppressed, melting is confined to a narrow region in the core of the band.

Key words: adiabatic shear; localization; plasticity; fracture; melting; phase-field; iron; steel

1 Introduction

Shear localization is a prevalent failure mode in solid materials that undergo strain-softening mechanisms. In crystalline metals deformed at high rates, near-adiabatic conditions are obtained, promoting a build up of local internal energy and temperature from plastic work, in turn leading to

*Email: john.d.clayton1.civ@army.mil

thermal softening as dislocation mobility increases with temperature. A mechanical instability ensues, beyond which localization into a thin band of very high shear strain and strain rate occurs [1, 2]. Shear banding is often accompanied by damage mechanisms such as cracking and void growth [3–7], and melting is theoretically possible if temperatures become large enough [8]. In this work, “damage” and “ductile fracture” are used to refer changes in local material structure—distinct from phase transformation and deformation twinning and not captured by thermal softening alone in the context of continuum plasticity theory—that induce degradation of local strength.

Experiments and models on adiabatic shear spanning the previous four decades are reviewed in the monograph [1] and more recent article [2]. Most previous continuum modeling of adiabatic shear localization in metals, be it analytical [9–17] or numerical [18–24], did not explicitly address fracture or melting mechanisms. However, several continuum damage mechanics-type models for adiabatic shear [25–28] represented degradation distinctly from purely thermal softening. More recently, phase-field models [29–35], extending ideas for depicting brittle fracture and structural transformations in elastic solids [36–41], have addressed ductile fracture and adiabatic shear localization in elastic-plastic solids. A common element of many models is a contribution of some fraction of energy from plastic work to the net driving force for fracture [29–31, 33–35, 42], supported by experiments that show importance of microstructure- and damage-softening relative to thermal softening [43, 44]. Furthermore, many continuum damage and ductile-fracture phase-field models include a threshold inelastic energy density at which damage nucleates [27, 28, 33, 34, 45], as opposed to classical phase-field fracture mechanics wherein any elastic energy can initiate (diffuse) cracking [41, 46]. Timing of cracking or void nucleation relative to localized flow varies among metals with different compositions and microstructures [4–7, 47, 48]. Those cited experiments usually suggest that damage mechanisms accompany or follow localization, rather than precede it, since cracks and voids are scarcely seen outside shear bands in those materials tested.

Direct evidence of melting has been reported within dynamic shear bands in various titanium and steel alloys [47, 49–51]. Known prior analyses of adiabatic shear did not include the thermodynamics of melting, even though local temperatures far exceeding the melting point of iron or steel can be predicted inside the shear band [8, 11, 14, 52]. Phase-field models combining mechanics of elasticity and thermodynamics and kinetics of melting and solidification exist [53–56], but these do not consider plastic deformation or adiabatic shear. A continuum model described flowing material within a shear band using a Bingham model with Newtonian viscosity [57], at temperatures below the ambient melt temperature. Therein, the calibrated viscosity was so low for three different metallic systems that the constant, rate-independent part of the shear stress dominated.

A recent theoretical study [8] advanced the analyses of Molinari and Clifton [11, 12, 14] to account for influences of superposed pressure, external magnetic fields, and solid-solid phase transformations on adiabatic shear localization. Results showed how loading conditions and solid-solid phase transformations can promote or inhibit strain localization in iron and a high-strength Ni-Cr steel. Herein, treatments of Refs. [8, 11, 12, 14] are further extended to account for damage (i.e., ductile shear fracture) and melting (i.e., solid-liquid transformation) processes. Criteria for localization into a band of infinite shear [11] are analyzed, and methods for calculating the average shear strain at which localization ensues are developed. The latter require numerical iteration and numerical integration, as closed-form expressions for critical strain cannot be derived analyti-

cally. The ductile fracture component of the model further addresses the additional “average” shear strain accommodated by the sample after localization, accounting for the effective shear displacement jump across the band whose shear strain approaches infinity and width approaches zero. This allows for representation of a gradual softening behavior in the macroscopic shear stress versus shear strain response as regularly witnessed experimentally [5, 6, 28, 45, 58]. Overly abrupt drops to zero stress upon localization [8, 11, 12] were criticized by Molinari and Clifton [12] as a notable deficiency of their original approach, therein speculated a result of poor resolution of defects.

As assumed or justified in prior works [1, 8, 12, 59] for materials (e.g., steels) and average strain rates (e.g., $10^3 - 10^4/s$) of present interest, regularization mechanisms of heat conduction and inertia are omitted to enable a tractable analysis without recourse to advanced numerical methods such as finite elements or finite differences. Similarly, to allow localization into a damaged region of infinitesimal thickness, the ductile fracture component of the formulation omits gradient regularization of phase-field theory [60], and Newtonian viscosity of molten material is likewise omitted in the limit of singular surfaces [8, 11, 12, 61]. Any remaining (implicit) regularization is furnished by strain-rate sensitivity [62]. Results are thus interpreted as a limiting case: predictions would be expected to underestimate conditions for localization given the absence of other regularization mechanisms [1, 59]. An initial defect (e.g., strength perturbation) of greater intensity than imposed or predicted here and in Refs. [8, 11, 12] would be needed to instill the same post-peak shear strain.

This article consists of six more sections. In §2, a general 3-D continuum framework is outlined, including constitutive fundamentals and thermodynamics. In §3, specialization of the framework to simple shear and pressure loading is undertaken. Constitutive model components for viscoelasticity, ductile fracture, and melting are introduced in this context. In §4, localization criteria are examined, and methods of calculation of critical shear strain and average stress-strain response are explained. In §5, properties and results are reported for a high-strength steel and compared to experimental observation. In §6, effects of variations of material parameters on localization behaviors are explored. In §7, conclusions consolidate the main developments. Standard notation of continuum mechanics is used (e.g., Refs. [1, 63]), with vectors and tensors in bold font and scalars and scalar components in italics. A single Cartesian frame of reference is sufficient for this work.

2 3-D formulation

The general constitutive framework combines elements from Refs. [8, 29, 40, 53–55, 64–66]. Electromagnetic effects considered in Refs. [8, 64, 65] are excluded, but phase-field concepts for fracture [29, 40, 42, 66, 66] and melting [53–55] are now added. The material is isotropic in both solid polycrystalline and liquid amorphous states, and is assumed fully solid in its initial configuration.

Inertial dynamics, heat conduction, and surface energies are included the complete 3-D theory, as are thermal expansion and finite elastic shear strain. These features are retained in §2 for generality and to facilitate identification and evaluation of successive approximations made later. Furthermore, retainment of such physics in the general formulation will allow a consistent implementation of the complete nonlinear theory in subsequent numerical simulations, for potential future comparison to the results of semi-analytical calculations reported in §5 and §6.

2.1 Constitutive model

Denote the motion of a material particle at reference position \mathbf{X} by spatial coordinates $\mathbf{x} = \boldsymbol{\varphi}(\mathbf{X}, t)$. Gradients with respect to \mathbf{X} and \mathbf{x} are written $\nabla_0(\cdot)$ and $\nabla(\cdot)$, and a superposed dot denotes the time derivative at fixed \mathbf{X} . The deformation gradient \mathbf{F} and its determinant J are decomposed into a product of three terms [63, 67, 68], with \mathbf{F}^E thermoelastic deformation, \mathbf{F}^P plastic deformation from dislocation motion, and \mathbf{F}^I the total inelastic deformation from damage and melting:

$$\mathbf{F} = \nabla_0 \boldsymbol{\varphi} = \mathbf{F}^E \mathbf{F}^I \mathbf{F}^P, \quad J = \det \mathbf{F} = \det \mathbf{F}^E \det \mathbf{F}^I \det \mathbf{F}^P = J^E J^I J^P > 0. \quad (2.1)$$

None of $\mathbf{F}^E, \mathbf{F}^I, \mathbf{F}^P$ need be individually integrable to a vector field [69]. Denote dimensionless order parameter fields for melting by $\xi(\mathbf{X}, t) \in [0, 1]$ and damage by $\phi(\mathbf{X}, t) \in [0, 1]$, where

$$\xi \begin{cases} = 0 & \leftrightarrow & \text{solid material,} \\ \in (0, 1) & \leftrightarrow & \text{mixed phase region,} \\ = 1 & \leftrightarrow & \text{liquid material;} \end{cases} \quad \phi \begin{cases} = 0 & \leftrightarrow & \text{undamaged material,} \\ \in (0, 1) & \leftrightarrow & \text{partially degraded material,} \\ = 1 & \leftrightarrow & \text{fully degraded material.} \end{cases} \quad (2.2)$$

Deformations of solid and liquid phases are not tracked individually at a point \mathbf{X} , so each is effectively assigned the same overall deformation gradient $\mathbf{F}(\mathbf{X}, t)$ at time t . Accordingly, ξ is interpreted equivalently as the local mass fraction or local volume fraction of molten material. On the other hand, ϕ need not represent the local volume fraction of voids or free volume, but rather is a generic indicator of local strength loss.

In a body of reference volume Ω_0 , reference conditions are $\xi(\mathbf{X}) = \phi(\mathbf{X}) = 0 \forall \mathbf{X} \in \Omega_0$. Calculations do not consider bodies with initial liquid phases or with initial damage represented by nonzero values of $\xi(\mathbf{X}, 0)$ and $\phi(\mathbf{X}, 0)$, respectively. If the material contains initial defects associated with damage entities (e.g., pores, micro-cracks, or other intrinsically weak zones), $\phi(\mathbf{X}, t)$ represents only the additional damage incurred after loading begins, potentially nonzero only for $t > 0^+$. In §3.3, a relationship between initial strength perturbation $\delta\chi_0(\mathbf{X})$ and an initial damage variable physically analogous to, but mathematically distinct from, $\phi(\mathbf{X}, 0) = 0$, is introduced.

Deformation \mathbf{F}^I is a function of state (i.e., of order parameters), plasticity is isochoric, and symmetric thermoelastic deformation is measured by \mathbf{C}^E with isochoric part $\tilde{\mathbf{C}}^E$:

$$\mathbf{F}^I = \mathbf{F}^I(\xi, \phi); \quad J^P = \det \mathbf{F}^P = 1; \quad \mathbf{C}^E = (\mathbf{F}^E)^T \mathbf{F}^E, \quad \tilde{\mathbf{C}}^E = J^{E-2/3} \mathbf{C}^E. \quad (2.3)$$

Denote by $\chi(\mathbf{X}, t)$ a scalar internal state variable field associated with plastic deformation processes (e.g., a dimensionless measure of dislocation density). Let $\theta(\mathbf{X}, t)$ be absolute temperature. Helmholtz free energy per unit reference volume of the solid is ψ , consisting of thermoelastic strain energy W , thermal energy Q , microstructure energy R , and gradient surface energy Λ :

$$\psi(\mathbf{C}^E, \theta, \xi, \phi, \chi, \nabla_0 \xi, \nabla_0 \phi) = W(\mathbf{C}^E, \theta, \xi, \phi) + Q(\theta, \xi) + R(\xi, \phi, \chi) + \Lambda(\xi, \phi, \nabla_0 \xi, \nabla_0 \phi). \quad (2.4)$$

Denote by θ_0 a reference temperature and $\Delta\theta = \theta - \theta_0$. Non-degraded isothermal bulk modulus B_0 is assumed the same in solid and liquid phases for neutral and compressive states wherein

$\ln J^E \leq 0$. Volumetric coefficient of thermal expansion A_0 is assumed the same in solid and liquid. The non-degraded shear modulus of the solid is μ_0 . Thermoelastic strain energy combines a logarithmic equation of state [70, 71] with a polyconvex shear contribution [60]:

$$W(J^E, \tilde{\mathbf{C}}^E, \theta, \xi, \phi) = \frac{1}{2}B(\xi, \phi)(\ln J^E)^2 \left[1 - \frac{1}{3}(B'_0 - 2) \ln J^E\right] - A_0 B \Delta \theta \ln J^E + \frac{1}{2}\mu(\xi, \phi)(\text{tr} \tilde{\mathbf{C}}^E - 3). \quad (2.5)$$

Let $\iota^\xi(\xi) \in [0, \iota_1^\xi]$ be an interpolation function between solid and liquid states satisfying $\iota^\xi(0) = 1, \iota^\xi(1) = \iota_1^\xi \in [0, 1]$. Let $\bar{\omega}(\phi, J^E) = 1 + [\omega(\phi) - 1]H(\ln J^E) \in [0, 1]$ be a degradation function satisfying $\omega(0) = 1, \omega(1) = \omega_1 \in [0, 1]$, where $H(\cdot)$ is the left-continuous Heaviside function. Moduli are interpolated as follows, noting as $\xi \rightarrow 1$ and $\phi \rightarrow 1, B \rightarrow B_0 \omega_1 \iota_1^\xi$ in tension and $\mu \rightarrow \mu_0 \omega_1 \iota_1^\xi$:

$$B(\xi, \phi, J^E) = B_0 \bar{\omega}(\phi, J^E) [1 + \{\iota^\xi(\xi) - 1\}H(\ln J^E)], \quad \mu(\xi, \phi) = \mu_0 \omega(\phi) \iota^\xi(\xi). \quad (2.6)$$

Constants ω_1 or ι_1^ξ , when nonzero, enable remnant strength when a material element is fully fractured or melted, and $B = B_0$ in compression. Cauchy pressure p and deviatoric Cauchy stress $\tilde{\boldsymbol{\sigma}}$ then follow from (2.5), with $\tilde{\mathbf{B}}^E$ the spatial deviatoric lattice strain:

$$\begin{aligned} \boldsymbol{\sigma} &= \tilde{\boldsymbol{\sigma}} - p\mathbf{1}; \quad p = -\frac{1}{3}\text{tr} \boldsymbol{\sigma} = -\frac{1}{J} \frac{\partial \psi}{\partial \ln J^E} = -\frac{B}{J} \left\{ \ln J^E \left[1 - \frac{1}{2}(B'_0 - 2) \ln J^E\right] - A_0 \Delta \theta \right\}; \quad (2.7) \\ \tilde{\boldsymbol{\sigma}} &= \frac{2}{J} \mathbf{F}^E \frac{\partial \psi}{\partial \tilde{\mathbf{C}}^E} : \frac{\partial \tilde{\mathbf{C}}^E}{\partial \mathbf{C}^E} (\mathbf{F}^E)^\text{T} = \frac{\mu}{J} \tilde{\mathbf{B}}^E, \quad \tilde{\mathbf{B}}^E = (J^E)^{-2/3} \mathbf{F}^E (\mathbf{F}^E)^\text{T} - \frac{1}{3} \text{tr} [(J^E)^{-2/3} \mathbf{F}^E (\mathbf{F}^E)^\text{T}] \mathbf{1}. \end{aligned} \quad (2.8)$$

Specific heat per unit volume c_V is assumed the same for solid and liquid phases and is idealized as independent of θ . Latent heat of fusion per unit reference volume of the solid is the constant h_T , positive for the usual case of higher energy of the liquid than the solid coexisting at the same (p, θ) . Herein $h_T \geq 0$. An equilibrium transformation temperature is the constant θ_T . At this temperature, in the absence of elastic deformation, stored energy of microstructure, and gradient surface energy, the free energy densities of solid and liquid phases are equal, whereby θ_T is interpreted as the melt temperature. Thermal energy is

$$Q(\theta, \xi) = -c_V [\theta \ln(\theta/\theta_0) - \Delta \theta] + [(h_T/\theta_T)(\theta - \theta_T)] \iota^\xi(\xi). \quad (2.9)$$

Denote by $\theta_I \leq \theta_T$ a melt instability temperature and the constant $A_\xi = 3h_T(1 - \theta_I/\theta_T) \geq 0$ [53].

Denote by $E_C \geq 0$ the cohesive energy per unit reference volume [40, 60], presumed matching in solid and liquid phases here for simplicity. More generally, E_C could depend on ξ and θ , to allow for different, temperature-dependent cavitation thresholds in solid and liquid. However, data to justify such generalizations, incurring additional driving and resistive forces for melting and fracture and increasing model complexity and computational burden, appear difficult to measure and do not seem to exist for the material analyzed in §5. Microstructure energy is

$$R(\xi, \phi, \chi) = \mu_0 [1 - \iota_0^\xi \{1 - \iota^\xi(\xi)\}] \bar{R}(\chi) + A_\xi \xi^2 (1 - \xi)^2 + E_C f_\phi(\phi), \quad (2.10)$$

with \bar{R} a dimensionless function of χ . The first term on the right in (2.10), for stored energy of dislocations, is scaled by the shear modulus [63], the second is a double-well for phase boundaries [53–55], and the third, with $f_\phi(\phi) \in [0, 1]$ a dimensionless function, is for homogeneous fracture [40, 66]. Constant $r_\xi^0 \in [0, 1]$ is the fraction of stored energy of cold work released upon melting.

Let Γ_ξ and Γ_ϕ be surface energies for solid-liquid boundaries and cracks, respectively, and let l_ξ, l_ϕ be regularization length constants. Gradient energy of internal surfaces is then the usual sum of quadratic forms [53, 66], where here surface energies can generally depend on order parameters:

$$\Lambda(\xi, \phi, \nabla_0 \xi, \nabla_0 \phi) = \Gamma_\xi(\phi) l_\xi |\nabla_0 \xi|^2 + \Gamma_\phi(\xi) l_\phi |\nabla_0 \phi|^2. \quad (2.11)$$

Surface tension [53–55] is omitted from R and Λ for brevity and simplicity; it could be included by multiplying right sides of (2.10) and (2.11) by J and replacing $\nabla_0(\cdot)$ with $\nabla(\cdot)$ in (2.11).

For later use, define first Piola-Kirchhoff stress \mathbf{P} , elastic second Piola-Kirchhoff stress \mathbf{S} , Mandel stress $\bar{\mathbf{S}}$, and the thermoelastic entropy constitutive relation as

$$\mathbf{P} = J \boldsymbol{\sigma} \mathbf{F}^{-T}, \quad \mathbf{S} = J(\mathbf{F}^E)^{-1} \boldsymbol{\sigma} (\mathbf{F}^E)^{-T} = 2 \partial \psi / \partial \mathbf{C}^E, \quad \bar{\mathbf{S}} = \mathbf{C}^E \mathbf{S}, \quad \eta = -\partial \psi / \partial \theta. \quad (2.12)$$

With η and U being entropy and internal energy per unit volume, \mathbf{q} the referential heat flux, and $\kappa \geq 0$ isotropic Fourier conductivity generally dependent on temperature, phase, and damage:

$$U = \psi + \theta \eta, \quad \mathbf{q}(\xi, \phi, \theta, \nabla_0 \theta) = -\kappa(\xi, \phi, \theta) \nabla_0 \theta. \quad (2.13)$$

2.2 Balance laws and dissipation

Standard local forms [63, 71] for conservation of mass and momentum are invoked, where ρ_0 and ρ are referential (solid, undeformed and undamaged) and spatial (deformed, possibly molten, and possibly damaged) mass densities, \mathbf{b} is body force per unit mass, and $\mathbf{v} = \dot{\mathbf{x}}$ is particle velocity:

$$\rho_0 = \rho J, \quad \nabla \cdot \boldsymbol{\sigma} + \rho \mathbf{b} = \rho \dot{\mathbf{v}}, \quad \boldsymbol{\sigma} = \boldsymbol{\sigma}^T. \quad (2.14)$$

Let \mathbf{n}_0 be the unit outward normal to material body Ω_0 on external boundary $\partial \Omega_0$. Global forms of the balance of energy and entropy inequality are as follows, the first extending classical continuum mechanics to account for surface energetics of order parameters [60, 66, 72]:

$$\begin{aligned} \frac{d}{dt} \int_{\Omega_0} U d\Omega_0 + \frac{d}{dt} \int_{\Omega_0} \frac{\rho_0}{2} |\mathbf{v}|^2 d\Omega_0 &= \oint_{\partial \Omega_0} (\mathbf{P} \cdot \mathbf{n}_0) \cdot \mathbf{v} d\partial \Omega_0 - \oint_{\partial \Omega_0} (\mathbf{q} \cdot \mathbf{n}_0) d\partial \Omega_0 \\ &\quad + \oint_{\partial \Omega_0} \left(\frac{\partial \psi}{\partial \nabla_0 \xi} \cdot \mathbf{n}_0 \right) \dot{\xi} d\partial \Omega_0 + \oint_{\partial \Omega_0} \left(\frac{\partial \psi}{\partial \nabla_0 \phi} \cdot \mathbf{n}_0 \right) \dot{\phi} d\partial \Omega_0, \end{aligned} \quad (2.15)$$

$$\frac{d}{dt} \int_{\Omega_0} \eta d\Omega_0 + \oint_{\partial \Omega_0} \frac{\mathbf{q} \cdot \mathbf{n}_0}{\theta} d\partial \Omega_0 \geq 0. \quad (2.16)$$

The divergence theorem, (2.14), and differentiability gives local versions of (2.15) and (2.16):

$$\dot{U} = \mathbf{P} : \dot{\mathbf{F}} - \nabla_0 \cdot \mathbf{q} + \nabla_0 \cdot [(\partial \psi / \partial \nabla_0 \xi) \dot{\xi} + (\partial \psi / \partial \nabla_0 \phi) \dot{\phi}], \quad (2.17)$$

$$\theta \dot{\eta} + \nabla_0 \cdot \mathbf{q} - (\mathbf{q} \cdot \nabla_0 \theta) / \theta \geq 0. \quad (2.18)$$

Define the internal dissipation as follows, applying the first of (2.13) and (2.17):

$$\mathfrak{D} = \theta \dot{\eta} + \nabla_0 \cdot \mathbf{q} = \mathbf{P} : \dot{\mathbf{F}} + \nabla_0 \cdot [(\partial \psi / \partial \nabla_0 \xi) \dot{\xi} + (\partial \psi / \partial \nabla_0 \phi) \dot{\phi}] - \dot{\psi} - \dot{\theta} \eta. \quad (2.19)$$

The second law (2.18) is, from (2.1), (2.3), (2.12), (2.13), and chain-rule differentiation of (2.4),

$$\mathfrak{D} + \frac{\kappa}{\theta} |\nabla_0 \theta|^2 \geq 0; \quad \mathfrak{D} = [(\mathbf{F}^I)^T \bar{\mathbf{S}} (\mathbf{F}^I)^{-T}] : \mathbf{L}^P + \zeta \dot{\xi} + \zeta \dot{\phi} + \vartheta \dot{\chi}, \quad \mathbf{L}^P = \dot{\mathbf{F}}^P \mathbf{F}^{P-1}; \quad (2.20)$$

$$\begin{aligned} \zeta &= -\partial \psi / \partial \xi + \nabla_0 \cdot (\partial \psi / \partial \nabla_0 \xi) + \mathbf{P} : (\partial \mathbf{F} / \partial \xi) \\ &= -\partial(W + Q + R + \Lambda) / \partial \xi + 2l_\xi \nabla_0 \cdot (\Gamma_\xi \nabla_0 \xi) + [\bar{\mathbf{S}} (\mathbf{F}^I)^{-T}] : (\partial \mathbf{F}^I / \partial \xi), \end{aligned} \quad (2.21)$$

$$\begin{aligned} \zeta &= -\partial \psi / \partial \phi + \nabla_0 \cdot (\partial \psi / \partial \nabla_0 \phi) + \mathbf{P} : (\partial \mathbf{F} / \partial \phi) \\ &= -\partial(W + R + \Lambda) / \partial \phi + 2l_\phi \nabla_0 \cdot (\Gamma_\phi \nabla_0 \phi) + [\bar{\mathbf{S}} (\mathbf{F}^I)^{-T}] : (\partial \mathbf{F}^I / \partial \phi), \end{aligned} \quad (2.22)$$

$$\vartheta = -\partial \psi / \partial \chi = -\mu_0 [1 - (1 - \iota^\xi) r_0^\xi] \partial \bar{R} / \partial \chi. \quad (2.23)$$

Expansion of $\dot{\eta} = -\frac{\partial \psi}{\partial \theta}$ with (2.9), and (2.17), then give the temperature rate, noting $c_V = -\theta \frac{\partial^2 \psi}{\partial \theta^2}$:

$$c_V \dot{\theta} = \mathfrak{D} + h_T \frac{\theta}{\theta_T} \frac{d\iota^\xi}{d\xi} \dot{\xi} - A_0 \theta \left[B \frac{J^E}{J^E} + \ln J^E \left\{ \frac{\partial B}{\partial \xi} \dot{\xi} + \frac{\partial B}{\partial \phi} \dot{\phi} \right\} \right] + \nabla_0 \cdot (\kappa \nabla_0 \theta). \quad (2.24)$$

3 Dynamic shear with pressure

The problem analyzed in §3–§6 is similar to that of Ref. [8]. However, magnetization and magnetic fields considered in that work are omitted here, as are solid-solid phase transformations. Instead, solid-liquid transformations and ductile fracture are now included. It is possible to posit a reduced set of governing equations for shear band analysis from the outset, without referencing the full 3-D constitutive model of §2 that encompasses thermoelasticity, conduction, gradient regularization, and inertia. However, that full formulation is used as a starting point here to clarify the simplifying assumptions needed for mathematically tractable limit analysis in later sections.

3.1 Geometry, loading conditions, and governing equations

Shown in Fig. 1 is the transient boundary value problem of present study. Let (X, Y, Z) and (x, y, z) be Cartesian reference and spatial coordinates. The material domain Ω_0 is of initial height h_0 and current height $h(t)$. The slab is infinitely extended in X, x - and Z, z - directions. The following mixed boundary conditions are invoked. Denote by $v_x = v_0$ a constant velocity at $y = h$, with vanishing velocity $v_x = 0$ at $y = 0$. Constant pressure field $t_n = -p_0$ is applied as normal traction on all boundaries for $t \geq 0^+$. Though not depicted in Fig. 1, tangential traction from σ_{xy} at each cross section $x = \text{constant}$ exists. Letting (X, Y, Z) be coordinates *minus* application of p_0 , h_0 can be unequal to the Y value of the planar boundary of the stress-free slab due to compressibility (i.e., h_0 depends on p_0). Pressure p_0 is applied slowly so is treated as an isothermal and quasi-static pre-loading. Then for dynamic shearing when $t \geq 0^+$, $y = 0$ and $y = h$ are thermally insulated.

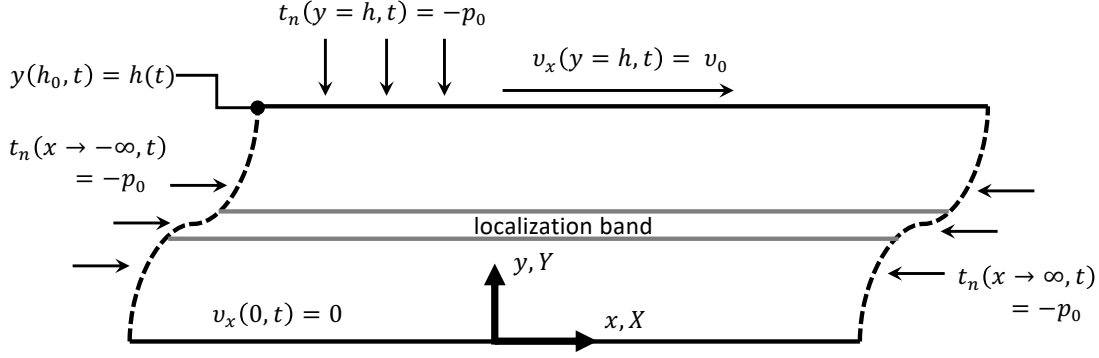


Figure 1. Boundary value problem for simple shear with superposed static pressure: tangential velocity at $y = h$ is v_0 , normal traction t_n is p_0 , including $t_n(z \rightarrow \pm\infty, t) = -p_0$. Slab is infinite in X, x, Z, z directions; initial (current) height of slab is h_0 (h). Slab is thermally insulated: $\partial\theta/\partial y = 0$ at $y = 0$ and at $y = h$ for $t \geq 0^+$. Initial variable $\chi_0(y) = \chi(y, t = 0)$ and temperature $\theta(y, t = 0)$ can vary modestly over $y \in (0, h)$.

For $t > 0^+$, while the body is shearing, h may displace from h_0 to maintain $p_0 = \text{constant}$ at $y = h$. This would occur if a volume-changing structural change such as melting or void growth is driven by shear. Note v_0 is constant for $t \geq 0^+$: acceleration from a resting state to an initial velocity gradient is not modeled. For $t \geq 0^+$, with infinite x, z boundaries, spatial fields depend at most only on (y, t) , a common assumption in analytical studies of shear bands [1, 11–13, 73]:

$$\mathbf{v} = \mathbf{v}(y, t), \quad \mathbf{F} = \mathbf{F}(y, t), \quad \boldsymbol{\sigma} = \boldsymbol{\sigma}(y, t), \quad \theta = \theta(y, t), \quad [t \geq 0^+]. \quad (3.1)$$

Any single localization band, within which \mathbf{F} differs from most of the rest of the domain, is oriented as in Fig. 1, but multiple parallel bands are allowable. Properties and initial temperature are constant with respect to x and z but need not so with respect to y . Perturbations in initial strength and temperature [14] can trigger localization at critical y locations.

Reference configuration covered by (X, Y, Z) is a model construct for analysis and need not be attained in experimental practice. Pressure p_0 is removed instantly at fixed θ from an unsheared state, before $v_x = v_0$ is applied. By construction, $\mathbf{F} = \mathbf{F}^E = \mathbf{F}^I = \mathbf{F}^P = \mathbf{1}$, $\boldsymbol{\sigma} = \mathbf{0}$, and $\phi = \xi = 0$ in this reference configuration. Almost everywhere, $\theta \approx \theta_0 = \text{constant}$ and $\chi \approx \chi_0 = \text{constant}$. Initial perturbations in θ and χ are permitted, with magnitudes so small that initial perturbations in J , p , ϕ , and ξ can be omitted.

Since the constitutive model of §2 is isotropic, the only nonzero Cauchy stress components are σ_{xx} , σ_{yy} , σ_{zz} , and $\sigma_{xy} = \sigma_{yx}$, and the nonzero heat flux component is q_Y . Taking $\mathbf{b} = \mathbf{0}$ henceforth and using (3.1), the second of (2.14) and heat conduction expressions in (2.13) and (2.24) are

$$\frac{\partial \sigma_{xy}}{\partial y} = \rho \dot{v}_x, \quad \frac{\partial \sigma_{yy}}{\partial y} = \rho \dot{v}_y; \quad (3.2)$$

$$q_Y = -\kappa F_{yY} \frac{\partial \theta}{\partial y}, \quad \nabla_0 \cdot \kappa \nabla_0 \theta = F_{yY} \frac{\partial}{\partial y} \left(\kappa F_{yY} \frac{\partial \theta}{\partial y} \right). \quad (3.3)$$

Regarding the deformation gradient, non-vanishing components of $\mathbf{F}(y(Y, t), t)$ are F_{xX} , F_{yY} , F_{zZ} and F_{xY} . For generic function $f = f(y(Y, t), t)$ (e.g., (3.1)), $\partial f / \partial Y = (\partial f / \partial y) F_{yY}$, and $\partial f / \partial X =$

$\partial f/\partial Z = 0$. From the second of (3.1), compatibility conditions [69] $\nabla_0 \times \mathbf{F} = \mathbf{0}$ necessitate

$$\partial F_{xx}/\partial Y = \partial F_{xy}/\partial X = 0, \quad \partial F_{zz}/\partial Y = \partial F_{zy}/\partial Z = 0. \quad (3.4)$$

Forms of $\boldsymbol{\varphi}$, \mathbf{F}^E , \mathbf{F}^ξ , and \mathbf{F}^P satisfying (3.4) are postulated a priori [8], based on Fig. 1. The reference configuration is unstressed, and \mathbf{F}^E includes the isothermal elastic volume change from initial pressurization by p_0 . Motion $\mathbf{x} = \boldsymbol{\varphi}(\mathbf{X}, t)$ and deformation gradient terms, written in 3×3 matrix format, are

$$x = x(X, Y, t), \quad y = y(Y, t), \quad z = z(Z, t); \quad \gamma = J^I \gamma^E + \gamma^J + \gamma^P; \quad (3.5)$$

$$[\mathbf{F}^E(Y, t)] = (J^E(t))^{1/3} \begin{bmatrix} 1 & \gamma^E(Y, t) & 0 \\ 0 & 1 & 0 \\ 0 & 0 & 1 \end{bmatrix}, \quad [\mathbf{F}^J(Y, t)] = \begin{bmatrix} 1 & \gamma^J(Y, t) & 0 \\ 0 & J^J(Y, t) & 0 \\ 0 & 0 & 1 \end{bmatrix}, \quad (3.6)$$

$$[\mathbf{F}^P(Y, t)] = \begin{bmatrix} 1 & \gamma^P(Y, t) & 0 \\ 0 & 1 & 0 \\ 0 & 0 & 1 \end{bmatrix}, \quad [\mathbf{F}(Y, t)] = \begin{bmatrix} 1 & \gamma(Y, t) & 0 \\ 0 & J^J(Y, t) & 0 \\ 0 & 0 & 1 \end{bmatrix} (J^E(t))^{1/3}. \quad (3.7)$$

The thermoelastic term \mathbf{F}^E contains spatially homogeneous volume change J^E and shear γ^E . The total shear *after* thermoelastic volume change in the last of (3.7) is γ . Plastic deformation is a simple shear γ^P . Inelastic deformation from damage and melting consists of simple shear γ^J and strain normal to the band, with volume change J^J , both interpolated as follows [39, 53, 66]:

$$\gamma^J(\xi, \phi) = \gamma^\xi(\xi) + \gamma^\phi(\phi), \quad \gamma^\xi = \gamma_0^\xi (1 - \iota^\xi(\xi)), \quad \gamma^\phi = \gamma_0^\phi (1 - \iota^\phi(\phi)); \quad (3.8)$$

$$J^J(\xi, \phi) = J^\xi(\xi) J^\phi(\phi) = \frac{J^\xi(\xi)}{1/J^\phi(\phi)} = \frac{1 + \delta_0^\xi (1 - \iota^\xi(\xi))}{1 - \delta_0^\phi (1 - \iota^\phi(\phi))}; \quad (1 - \iota_1^\xi) \delta_0^\xi = \frac{\rho^{(0)}}{\rho^{(1)}} - 1. \quad (3.9)$$

Interpolation functions between solid and liquid, and between undamaged and failed states, are

$$\begin{aligned} \iota^\xi(\xi) &\in [0, \iota_1^\xi], & \iota^\phi(\phi) &\in [0, \iota_1^\phi]; \\ \iota^\xi(0) &= \iota^\phi(0) = 1; & \iota^\xi(1) &= \iota_1^\xi \in [0, 1], & \iota^\phi(1) &= \iota_1^\phi \in [0, 1]. \end{aligned} \quad (3.10)$$

Material constants are $\gamma_0^\xi, \gamma_0^\phi, \delta_0^\xi$, and δ_0^ϕ , any of which can be zero, positive, or negative. These constants are multiplied by $1 - \iota_1^\xi$ or $1 - \iota_1^\phi$ to give any structure change-induced shear strains and volume changes at $\xi = 1$ or $\phi = 1$. Mass densities of solid and fully liquid states are $\rho^{(0)}$ and $\rho^{(1)}$, respectively. When damage manifests physically as induced cavities or pores, then the quantity $(1 - \iota_1^\phi) \delta_0^\phi$ can be interpreted as the void volume fraction at the locally failed state. Notice that J^ϕ accounts only for volume changes induced during deformation, and not for effects of initial defects (e.g., J^ϕ does not account for initial porosity independent of ϕ that is implicitly included in $\rho^{(0)}$).

Inserting \mathbf{F}^E of (3.6), the Cauchy stress of (2.7) and (2.8) becomes

$$[\boldsymbol{\sigma}] = \frac{1}{J^E J^J} \begin{bmatrix} -\tilde{p} + \frac{2}{3} \mu (\gamma^E)^2 & \mu \gamma^E & 0 \\ \mu \gamma^E & -\tilde{p} - \frac{1}{3} \mu (\gamma^E)^2 & 0 \\ 0 & 0 & -\tilde{p} - \frac{1}{3} \mu (\gamma^E)^2 \end{bmatrix}, \quad (3.11)$$

$$\tilde{p}(J^E, \theta) = -B \{ \ln J^E [1 - \frac{1}{2} (B'_0 - 2) \ln J^E] - A_0 (\theta - \theta_0) \}. \quad (3.12)$$

Three approximations are introduced to simplify (3.11) and (3.12) [8]. First, elastic shear is assumed small so terms of $O((\gamma^E)^2)$ are negligible. Second, thermal expansion in \bar{p} is omitted (e.g., $A_0 \rightarrow 0$), typical in analysis of shear bands [1, 11, 12, 73]. Third, terms of $O(\delta_0^\xi)$, $O(\delta_0^\phi)$ are omitted in the prefactor of (3.11). This implies local volume changes from melting and porosity remain small. For ferrous metals studied in §5 and §6, such volume changes, both expansive, cannot exceed $\approx 5\%$, which would lead to overestimation of stress, at most, by the same percentage. Thus, (3.11) reduces to

$$[\boldsymbol{\sigma}] \approx \begin{bmatrix} -p_0 & \mu\gamma^E/J^E & 0 \\ \mu\gamma^E/J^E & -p_0 & 0 \\ 0 & 0 & -p_0 \end{bmatrix}, \quad J^E \approx \arg_{J^E > 0} \{p_0 = -B_0 \frac{\ln J^E}{J^E} [1 - \frac{1}{2}(B'_0 - 2) \ln J^E]\}. \quad (3.13)$$

Since $p \approx p_0 = \text{constant}$, $J^E(p_0) = \text{constant}$ for $t \geq 0^+$, consistent with (3.1).

Initial pressure, if tensile, is assumed small enough that no damage is incurred prior to shear loading, and subsequently, changes in B from shear-induced melting and fracture are ignored in the second of (3.13). Transient increases to J^E that would be needed to offset reduction of B with increasing ϕ when $p_0 < 0$ are omitted. Thus, (3.13) is most accurate for neutral or compressive states with $p_0 \geq 0$. Since $\sigma_{yy} \approx -p_0$, the second of (3.2) is now obeyed unconditionally when $\dot{v}_y = 0$. The first of (3.2) is $\partial \tau / \partial y \approx \partial(\mu\gamma^E) / \partial y = J^E \rho \dot{v}_x$. If $\tau(t) = J^E \sigma_{xy}(t)$ is independent of y , then inertial force is negligible.

From (3.6)–(3.13), the dissipation contributions from plastic and inelastic structure deformations of melting and fracture in the energy balance of (2.24) and entropy inequality of (2.20) are

$$[(\mathbf{F}^I)^T \bar{\mathbf{S}}(\mathbf{F}^I)^{-T}] : \mathbf{L}^P = \tau \dot{\gamma}^P, \quad \tau = J^E \sigma_{xy} = \mu\gamma^E/J^I \approx \mu\gamma^E, \quad \bar{p}_0 = J^E p_0; \quad (3.14)$$

$$[\bar{\mathbf{S}}(\mathbf{F}^I)^{-T}] : \frac{\partial \mathbf{F}^I}{\partial \xi} \dot{\xi} = - \left[\tau \gamma_0^\xi - \frac{\{\bar{p} - \frac{2}{3}\mu(\gamma^E)^2\} \delta_0^\xi}{1 + \delta_0^\xi(1 - \iota^\xi)} \right] \frac{d\iota^\xi}{d\xi} \dot{\xi} \approx - [\tau \gamma_0^\xi - \bar{p}_0 \delta_0^\xi] \frac{d\iota^\xi}{d\xi} \dot{\xi}, \quad (3.15)$$

$$[\bar{\mathbf{S}}(\mathbf{F}^I)^{-T}] : \frac{\partial \mathbf{F}^I}{\partial \phi} \dot{\phi} = - \left[\tau \gamma_0^\phi - \frac{\{\bar{p} - \frac{2}{3}\mu(\gamma^E)^2\} \delta_0^\phi}{1 - \delta_0^\phi(1 - \iota^\phi)} \right] \frac{d\iota^\phi}{d\phi} \dot{\phi} \approx - [\tau \gamma_0^\phi - \bar{p}_0 \delta_0^\phi] \frac{d\iota^\phi}{d\phi} \dot{\phi}. \quad (3.16)$$

Conjugate forces ς and ζ of (2.21) and (2.22) become, with Γ_ξ and Γ_ϕ constants for brevity,

$$\begin{aligned} \varsigma \approx & -\mu_0 [\frac{1}{2} \omega(\text{tr} \tilde{\mathbf{C}}^E - 3) + r_0^\xi \bar{R}] \frac{d\iota^\xi}{d\xi} - 2A_\xi \xi (1 - \xi)(1 - 2\xi) - h_T [\theta / \theta_T - 1] \frac{d\iota^\xi}{d\xi} \\ & - [\tau \gamma_0^\xi - \bar{p}_0 \delta_0^\xi] \frac{d\iota^\xi}{d\xi} + 2l_\xi \Gamma_\xi \nabla_0^2 \xi, \end{aligned} \quad (3.17)$$

$$\zeta \approx -\mu_0 [\frac{1}{2} (\text{tr} \tilde{\mathbf{C}}^E - 3)] \iota^\xi \frac{d\omega}{d\phi} - E_C \frac{df_\phi}{d\phi} - [\tau \gamma_0^\phi - \bar{p}_0 \delta_0^\phi] \frac{d\iota^\phi}{d\phi} + 2l_\phi \Gamma_\phi \nabla_0^2 \phi. \quad (3.18)$$

Temperature rate (2.24) becomes, with generally transient Taylor-Quinney factor $\beta(y(Y, t), t)$ [74, 75], $\theta = \theta(y(Y, t), t)$, $J^E(p_0) = 0$, $A_0 = 0$, and $\kappa = \text{constant}$ for brevity and simplicity,

$$c_V \dot{\theta} \approx \beta \tau \dot{\gamma}^P + \left[\varsigma + h_T \frac{\theta}{\theta_T} \frac{d\iota^\xi}{d\xi} \right] \dot{\xi} + \zeta \dot{\phi} + \kappa \frac{\partial^2 \theta}{\partial Y^2}, \quad \beta = \frac{\tau \dot{\gamma}^P - \mu_0 [1 - (1 - \iota^\xi) r_0^\xi] (\frac{\partial \bar{R}}{\partial \chi}) \dot{\chi}}{\tau \dot{\gamma}^P}. \quad (3.19)$$

Here in (3.19), β accounts for stored energy of cold work but not energies of fracture and melting.

Let an arbitrary rigid body rotation be \mathbf{R}_0 . Strain energy W and stress $\boldsymbol{\sigma}$ are unaffected by transformations of the form $\mathbf{F}^E \rightarrow \mathbf{F}^E \mathbf{R}_0^T$ with $\mathbf{F}^I \mathbf{F}^P \rightarrow \mathbf{R}_0 \mathbf{F}^I \mathbf{F}^P$. Different choices of \mathbf{R}_0 can affect partitioning of dissipation among inelastic deformation mechanisms. Currently setting $\mathbf{R}_0 = \mathbf{1}$, motivated by physics specific to Fig. 1 and metal plasticity, is not arbitrary [63, 76].

3.2 Approximations and reduced governing equations

The following additional assumptions are implemented later to facilitate analysis, in conjunction with prior assumptions that $A_0 \rightarrow 0$, δ_0^ξ and δ_0^ϕ are small compared to unity, and $B \approx B_0 = \text{constant}$:

1. Inertia is omitted ($\dot{v}_x \rightarrow 0$), as in Refs. [8, 11, 12];
2. The shearing response is idealized as rigid-viscoplastic, as in Refs. [1, 8, 11, 12];
3. Gradient regularization is omitted ($l_\phi \rightarrow 0, l_\xi \rightarrow 0$) [40, 60], and $\theta_I \rightarrow \theta_T \Rightarrow A_\xi \rightarrow 0$;
4. Heat conduction is omitted ($\kappa \rightarrow 0$), as in Refs. [8, 11, 12];
5. Taylor-Quinney factor is constant ($\beta \dot{\gamma}^P \rightarrow \beta_0 \dot{\gamma}, \beta_0 = \text{constant} \in (0, 1]$), as in Refs. [8, 11, 12].

From the first assumption, the lone non-trivial equilibrium equation in the first of (3.2) becomes

$$\frac{\partial \tau(y, t)}{\partial y} = 0 \quad \Rightarrow \quad \frac{\partial \tau(y(Y, t), t)}{\partial Y} = F_{yY} \frac{\partial \tau}{\partial y} = 0 \quad \Rightarrow \quad \tau_A = \tau(Y_A, t) = \tau(Y_B, t) = \tau_B. \quad (3.20)$$

Coordinates of any two material points the slab with shear stresses τ_A, τ_B are written Y_A, Y_B . Recall $\tau = J^E \sigma_{xy} \approx \mu \gamma^E$ and from (3.6) and (3.7) that $F_{yY}(Y, t) = (J^E)^{1/3} J^I(Y, t) > 0$. Physical suitability of the first and fourth assumptions (i.e., omission of inertia and conduction) for materials and loading conditions of present interest, namely steels deformed in torsion at rates $\dot{\gamma} \in [10^3/\text{s}, 10^4/\text{s}]$ is discussed in Refs. [1, 8, 11, 12, 59]. Limitations of these assumptions are reconsidered in §5.2 and §7. Acceleration is more important at much higher rates, conduction at much lower rates.

From the second assumption above, rigid viscoplasticity sets $\tau/\mu \rightarrow 0$ but τ can remain finite. Consistent with this limit, $\gamma^E \rightarrow 0$, $\tau/\mu_0 \rightarrow 0$, $\tau \rightarrow 0$ as $\iota^\xi \omega \rightarrow 0$, and quadratic deviatoric strain energy $\mu(\text{tr} \tilde{\mathbf{C}}^E - 3) \rightarrow 0$. With J^I on the order of unity, the shear strain and shear strain rate, with explicit viscoplastic and inelastic structural deformations, reduce to

$$\gamma \approx \gamma^P + \gamma_0^\xi (1 - \iota^\xi) + \gamma_0^\phi (1 - \iota^\phi) \geq 0, \quad \dot{\gamma} \approx \dot{\gamma}^P - \gamma_0^\phi \frac{d\iota^\phi}{d\phi} \dot{\phi} - \gamma_0^\xi \frac{d\iota^\xi}{d\xi} \dot{\xi} \geq 0. \quad (3.21)$$

If $\gamma^\xi + \gamma^\phi < 0$, shearing from slip must exceed that from fracture and melting. If $\gamma^\xi + \gamma^\phi > 0$, then $\gamma^P < 0$ is not impossible.

The third assumption discards some energetic contributions of boundary layers between solid and liquid and between undamaged and fully fractured material. While this assumption neglects certain physics resolved by phase-field theories of gradient type [41, 53, 54, 66], it allows for modeling of spatial discontinuities in order parameters, and thus does not implicitly forbid jumps in shear strain γ and temperature θ needed for the locally infinite- γ description of adiabatic shear bands [8, 11, 12, 14] invoked in §4–§6. Were the gradient energy contribution from ξ included, a

sharp spatial change or jump in ξ would be impossible due to the nearly infinite or infinite energetic barrier from Λ of (2.11). A similar remark applies for the gradient energy contribution from ϕ in (2.11). Since primary driving forces for local increases in ξ and ϕ are later identified with θ and γ , respectively, the same barriers could restrict large increases in θ and γ to zones or bands of finite width. A jump to an extreme value of θ or γ for material in an infinitesimal-width band relative to its surroundings would engender a discontinuity in ξ or ϕ that is inadmissible in a gradient-regularized theory. Conductivity $\kappa > 0$ would also restrict the minimum width of a shear band to avoid infinite contributions to dissipation in (2.20) and temperature rate in (3.19), as temperature gradients approach infinite magnitudes. Combining the third assumption with the second,

$$\varsigma \approx - \left[\mu_0 r_0^\xi \bar{R} + h_T \{ \theta / \theta_T - 1 \} + \tau \gamma_0^\xi - \bar{p}_0 \delta_0^\xi \right] \frac{d\iota^\xi}{d\xi}, \quad \zeta \approx -E_C \frac{df_\phi}{d\phi} - [\tau \gamma_0^\phi - \bar{p}_0 \delta_0^\phi] \frac{d\iota^\phi}{d\phi}. \quad (3.22)$$

Finally, from the fourth and fifth assumptions, the first inequality in (2.20), the first equality in (3.19), and the total cumulative plastic work W^P are approximated, respectively, by

$$\beta_0 \tau \dot{\gamma} + \varsigma \dot{\xi} + \zeta \dot{\phi} \gtrsim 0, \quad c_V \dot{\theta} \approx \beta_0 \tau \dot{\gamma} + \left[\varsigma + h_T \frac{\theta}{\theta_T} \frac{d\iota^\xi}{d\xi} \right] \dot{\xi} + \zeta \dot{\phi}, \quad W^P \approx \int_0^t \tau \dot{\gamma} d\hat{t} = \int_0^\gamma \tau d\hat{\gamma}. \quad (3.23)$$

From (3.21) with $\dot{\gamma}^E = 0$, if $\gamma_0^\xi \dot{\xi} \neq 0$ or $\gamma_0^\phi \dot{\phi} \neq 0$, then $\dot{\gamma}^P \neq \dot{\gamma}$. In that case, the fifth assumption implies $\beta = \beta(t) = \beta_0 (1 + \dot{\gamma}^P / \dot{\gamma}^I)$ can be transient if $\beta_0 = \text{constant}$, the latter implicitly affected by dissipative contributions from inelastic structural shears. In §5 and §6, $\gamma_0^\xi = \gamma_0^\phi = 0 \Rightarrow \beta \rightarrow \beta_0$.

Models for plasticity, ductile damage, and melting following in §3.3, §3.4, and §3.5 are specialized to the dynamic, adiabatic, pressurized simple shear problem of §3.1, simplifying assumptions of §3.2, and relatively strong, ductile polycrystalline metals like structural steels. Different models would be needed for other loading regimes and material classes (e.g., quasi-statics, brittle solids).

3.3 Viscoplasticity

A power-law viscoplastic flow rule [8, 11–13] relates $\dot{\gamma}$ to Kirchhoff shear stress $\tau = J^E \sigma_{xy} \geq 0$:

$$\dot{\gamma} = \dot{\gamma}_0 (\tau/g)^{1/m}, \quad g = g(\xi, \phi, \chi, \theta; p_0) = g_Y(\xi, \phi, p_0) h(\chi) \lambda(\theta). \quad (3.24)$$

Denoted by $\dot{\gamma}_0 = \text{constant} \geq 0$ and $m = \text{constant} > 0$ are a reference strain rate and rate sensitivity. Flow stress $g \geq 0$ consists of pressure-, phase-, and damage-dependent static yield stress $g_Y \geq 0$, strain hardening (or softening) function $h \geq 0$, and thermal softening (or hardening) function $\lambda \geq 0$.

Internal state variable change $\chi(t) - \chi_0$ is associated with strain hardening, most often linked to increases in dislocation density [63, 77]. For monotonically increasing $\gamma(t)$, the simplest realistic representation of χ associated with dislocations is, with initial value χ_0 close to unity,

$$\chi(y, t) = \chi_0(Y(y, t)) + \gamma(y, t), \quad \chi_0 \approx 1; \quad \dot{\chi} = \dot{\gamma} \Rightarrow \bar{R} \approx \frac{1 - \beta_0}{\mu_0} \int_0^\gamma \frac{\tau d\hat{\gamma}}{1 - (1 - \iota^\xi) r_0^\xi} + \bar{R}_0. \quad (3.25)$$

In the rightmost expression, obtained from (3.19) and the fifth assumption of §3.2 with $\beta_0 \approx \beta$, $\bar{R}_0(Y) \geq 0$ is an initial condition related to stored energy from initial dislocation density at Y .

Fractured or molten material is assumed to have degraded strength. Classical dislocation plasticity theory [63, 77] presumes g_Y is proportional to shear modulus μ . Thus g_Y is interpolated akin to μ in (2.6) via functions $\iota^\xi(\xi)$ and $\omega(\phi)$. As in Refs. [8, 11–13], h and λ are power-law forms:

$$g_Y(\xi, \phi, p_0) = g_0(p_0)\iota^\xi(\xi)\omega(\phi), \quad h(\chi(\gamma)) = \chi_0(1 + \gamma/\gamma_0)^n, \quad \lambda(\theta) = (\theta/\theta_0)^\nu. \quad (3.26)$$

Here, $g_0(p_0) > 0$ is strength of the solid with pressure scaling, while γ_0 , n , and ν are dimensionless constants. Strength depends linearly on p_0 via the pressure derivative of shear modulus, μ' [8]:

$$g_0(p_0) = [1 + (\mu'/\mu_0)p_0]g_0(0); \quad \mu' = (\partial\mu/\partial p)_{\theta=\theta_0, p=0}. \quad (3.27)$$

To avoid unnecessary complexity that would be eliminated by the rigid-viscoplastic assumption, pressure scaling of μ was omitted in elastic strain energy (2.5). Flow stress τ is, inverting (3.24),

$$\tau(\gamma(y,t), \dot{\gamma}(y,t), \xi(y,t), \phi(y,t), \theta(y,t); \chi_0(y), p_0) = \chi_0 g_0(p_0) \iota^\xi(\xi) \omega(\phi) \left(1 + \frac{\gamma}{\gamma_0}\right)^n \left(\frac{\theta}{\theta_0}\right)^\nu \left(\frac{\dot{\gamma}}{\dot{\gamma}_0}\right)^m. \quad (3.28)$$

In metals, the strain hardening exponent n is usually positive, and thermal softening exponent ν is usually negative. These conventions are not enforced a priori as restrictions in the theory, however.

Accommodating usual degradation functions from continuum-damage [63, 64, 71, 78] and phase-field mechanics [41, 66] the function $\omega(\phi)$ first introduced in (2.6) and presently entering (3.26) is

$$\omega(\phi) = \omega_1 + (1 - \omega_1)(1 - \phi)^k, \quad d\omega/d\phi = -k(1 - \omega_1)(1 - \phi)^{k-1}. \quad (3.29)$$

Material constants are $k \geq 1$ and $\omega_1 \in [0, 1]$, recalling the latter for remnant strength at $\phi = 1$.

Initial deviation $\delta\chi_0(Y) = 1 - \chi_0(Y)$, if positive as assigned by convention in §4–§6, accounts for strength defects. These could be initial micro-cracks, pores [79], texture variations, weak interfaces at grain boundaries [74, 80], inclusions, or another microstructure feature that reduces strength. Deviation can be related to time-independent “damage” parameter $\tilde{\phi}_0$ with linear degradation function $\tilde{\omega}_0$:

$$\delta\chi_0(Y) = 1 - \chi_0(Y) = \tilde{\phi}_0(Y), \quad \tilde{\omega}_0(\tilde{\phi}_0) = 1 - \tilde{\phi}_0 = \chi_0. \quad (3.30)$$

This is akin to (3.29) with $\phi \rightarrow \tilde{\phi}_0$, $k \rightarrow 1$, and $\omega_1 \rightarrow 0$. In the present theory, it is advantageous to assign distinct values to $\tilde{\phi}_0$ and $\phi_0 = \phi(t=0)$, whereby $\phi_0 = 0$ is used as the standard initial condition. This allows $\tilde{\phi}_0$ and ϕ to describe different weakening mechanisms (e.g., grains locally oriented favorably for easy slip, unrelated to ductile fracture).

If the solid has mild rate sensitivity (i.e., m small versus unity), an assumption used in some, but not all, steps of prior analyses [8, 11, 12] replaces local strain rate in (3.28) with average $\dot{\gamma}$:

$$\tau(\gamma, \xi, \phi, \theta; \dot{\gamma}; \chi_0, p_0) \approx \chi_0 g_0(p_0) \iota^\xi(\xi) \omega(\phi) \left(1 + \frac{\gamma}{\gamma_0}\right)^n \left(\frac{\theta}{\theta_0}\right)^\nu \left(\frac{\dot{\gamma}}{\dot{\gamma}_0}\right)^m, \quad \dot{\gamma} = \frac{v_0}{h_0}. \quad (3.31)$$

More accurate (3.28) is used in the momentum balance. Approximation (3.31) is used to estimate dissipative contributions to temperature [11, 12] and structure kinetics [8] if $\dot{\gamma}(y,t)$ is unknown.

3.4 Shear fracture

Classical, elastic-brittle phase-field fracture models [37, 41, 81, 82] are inadequate for describing ductile failure in adiabatic shear bands because they do not account for coupling of plastic deformation to effective fracture toughness and fracture kinetics. Rather, similar to Refs. [29, 30, 33–35, 42, 83, 84], here some fraction of plastic working is used as a driving force for shear fracture.

Let $\alpha_0 \in [0, \chi_0]$ be a dimensionless constant quantifying this fraction. Degradation initiates when a threshold level of plastic work W^ϕ has been attained [27, 28, 33, 34, 83, 85]. Set $W^\phi = \chi_0 W_0^\phi [1 + (\mu'/\mu_0)p_0]$, where $W_0^\phi = \text{constant} \geq 0$. Accordingly, initial defects and tensile pressure are assumed to linearly reduce threshold W^ϕ , analogously to static yield-strength terms h and g_Y in (3.28) and (3.27). Ensuring net non-negative dissipation from plastic work and ductile fracture, the following kinetic law for the order parameter rate, $\dot{\phi}$, for dynamic shear degradation is postulated:

$$\begin{aligned} \zeta \dot{\phi} &= -[\alpha_0 \beta_0 / \chi_0] \tau \dot{\gamma} H(W^P - W^\phi) H(1 - \phi) \\ \Rightarrow \quad \beta_0 \tau \dot{\gamma} + \zeta \dot{\phi} &= \beta_0 \tau [1 - (\alpha_0 / \chi_0) H(W^P - W^\phi) H(1 - \phi)] \dot{\gamma} \geq 0. \end{aligned} \quad (3.32)$$

Heaviside function $H(1 - \phi)$ limits the solution to physical domain $\phi \in [0, 1]$. Substituting (3.22) into the first of (3.32) and enforcing $d\phi \geq 0$ gives a nonlinear differential equation at each $y \in [0, h]$:

$$\left[\left\langle E_C \frac{df_\phi}{d\phi} + \{ \tau(\phi, \cdot) \gamma_0^\phi - \bar{p}_0 \delta_0^\phi \} \frac{d\iota^\phi(\phi)}{d\phi} \right\rangle \right] d\phi = \left[\frac{\alpha_0 \beta_0}{\chi_0} \tau(\phi, \cdot) H(W^P - W^\phi) H(1 - \phi) \right] d\gamma, \quad (3.33)$$

where $\langle (\cdot) \rangle = \frac{1}{2} [(\cdot) + |(\cdot)|]$. The right side of (3.33) is non-negative since $\tau \geq 0$ and $d\gamma \geq 0$. The $\langle (\cdot) \rangle$ operation on the left ensures $d\phi \geq 0$ (i.e., irreversible damage), and $\phi \rightarrow 1$ by the $H(1 - \phi)$ factor on the right when resistance $-\zeta$ within $\langle (\cdot) \rangle$ on the left is non-positive. This equation must usually be integrated numerically for ϕ using (3.28) along with evolution equations for ξ and θ .

To demonstrate model features, apply (3.31) in each of (3.23) [8, 11, 12] and assume $\gamma_0^\phi = 0$, meaning no explicit inelastic shear strain from fracture. For monotonically increasing $\gamma(y, t)$, assume functional forms $\theta(y, t) = \theta(\gamma(y, t), y)$ and $\xi(y, t) = \xi(\gamma(y, t), y)$ exist. Denote by $\gamma_f(y)$ the value of $\gamma(y, t)$ at t when fracture initiates, as $W^P \rightarrow W^\phi$. Then (3.33) is separable and can be integrated for $\phi(\gamma) \in [0, 1]$ at fixed \bar{p}_0 , χ_0 , and y :

$$\int_0^\phi \left\langle \frac{E_C}{\omega(\hat{\phi})} \frac{df_\phi}{d\hat{\phi}} - \frac{\bar{p}_0 \delta_0^\phi}{\omega(\hat{\phi})} \frac{d\iota^\phi}{d\hat{\phi}} \right\rangle d\hat{\phi} = \alpha_0 \beta_0 g_0 \left(\frac{\dot{\gamma}}{\dot{\gamma}_0} \right)^m \int_{\gamma_f}^\gamma \iota^\xi(\xi(\hat{\gamma})) \left(1 + \frac{\hat{\gamma}}{\gamma_0} \right)^n \left(\frac{\theta(\hat{\gamma})}{\theta_0} \right)^v d\hat{\gamma}. \quad (3.34)$$

Now take $f_\phi = \phi$, $k = 1$ in (3.29), $\iota^\phi = 1 - \phi$, and assume $E_C + \bar{p}_0 \delta_0^\phi > 0$. Then (3.34) produces

$$\phi(\gamma) = \min \left[\frac{1 - \exp\{-A_f W_f^P(\gamma)\}}{1 - \omega_1}, 1 \right]; \quad A_f = \frac{\alpha_0 \beta_0 (1 - \omega_1)}{\chi_0 (E_C + \bar{p}_0 \delta_0^\phi)}, \quad W_f^P = \int_{\gamma_f}^\gamma \frac{\tau}{\omega} d\hat{\gamma}. \quad (3.35)$$

As plastic work $W_f^P \rightarrow \infty$, $\phi \rightarrow 1$. When $\gamma(y, t) \leq \gamma_f(y)$, the trivial solution is $\phi(y, t) = 0$, and $d\phi = 0$ when $\tau = 0$. Resistance to fracture at a given value of γ is afforded by E_C ; large α_0 , β_0 and defects $\delta\chi_0 = 1 - \chi_0 \geq 0$ promote fracture. If $E_C \leq \bar{p}_0 \delta_0^\phi$, with ductile damage expansive (i.e., $\delta_0^\phi > 0$) tensile pressure $-\bar{p}_0 \geq E_C / \delta_0^\phi$ causes fracture as soon as $W^P > W^\phi$ via $\phi \rightarrow 1$ in (3.33).

3.5 Melting

To ensure non-negative dissipation from melting or solidification, the Allen-Cahn or Ginzburg-Landau equation [53–55] is often invoked for kinetics of ξ , especially when modeling boundary layers of partially molten material. Here, since gradient regularization is omitted and solidification is less relevant, a linear relaxation model for phase transformations [64, 65, 86], also obeying non-negative dissipation, is instead adapted for melting. Letting $t_R^\xi \geq 0$ be a relaxation time constant,

$$t_R^\xi \dot{\xi} = \begin{cases} \langle \bar{\xi} - \xi \rangle, & (\varsigma > 0), \\ -\langle \xi - \bar{\xi} \rangle, & (\varsigma \leq 0) \end{cases} \Rightarrow \varsigma \dot{\xi} \geq 0. \quad (3.36)$$

The metastable melt fraction is $\bar{\xi}$. With $\alpha_\xi \geq 0$ and $\beta_\xi > 0$ kinetic barriers, the following ordinary differential equation (ODE) is posited for melting but not solidification, akin to Refs. [64, 65, 86]:

$$d\bar{\xi} = -t' d \left[\frac{\langle -\varsigma/t' - \alpha_\xi \rangle}{\beta_\xi} \right] H(1 - \bar{\xi}); \quad t'(\bar{\xi}) = \frac{dt^\xi(\bar{\xi})}{d\bar{\xi}} \leq 0, \quad t'(1) = 0. \quad (3.37)$$

The Heaviside function restricts the solution to $\bar{\xi} \leq 1$. This differential equation must generally be solved numerically for $\bar{\xi}$ since ς in (3.22) depends implicitly on $\bar{\xi}$. Dividing by t' and integrating,

$$\int_0^{\bar{\xi}} \frac{d\xi}{t'} = -\frac{1}{\beta_\xi} \langle \mu_0 r_0^\xi \bar{R} + \frac{h_T}{\theta_T} \{ \theta - \theta_T \} + \{ \tau \gamma_0^\xi - \bar{p}_0 \delta_0^\xi \} - \alpha_\xi \rangle, \quad (\bar{\xi} \leq 1). \quad (3.38)$$

Consider another analytical example to illustrate concepts and model features. When $t_R^\xi \dot{\gamma} \ll 1$, the left side of (3.36) is assumed to vanish, whereby $\xi \approx \bar{\xi}$. Assume such conditions hold, meaning melting completes at time scales fast relative to the loading time. Continuing to assume forms $\theta(\gamma(y,t), y)$ and $\phi(\gamma(y,t), y)$ akin to those in (3.34) exist, and choosing, for example,

$$t^\xi(\xi) = t_1^\xi + (1 - t_1^\xi)(1 - \xi)^2, \quad t' = dt^\xi/d\xi = -2(1 - t_1^\xi)(1 - \xi) \in [-2(1 - t_1^\xi), 0], \quad (3.39)$$

(3.38) can be solved analytically as

$$\xi(\gamma) = 1 - \exp \left[-\frac{2(1 - t_1^\xi)}{\beta_\xi} \langle \Xi(\gamma) \rangle \right], \quad \Xi = \frac{h_T}{\theta_T} \{ \theta - \theta_T \} + \mu_0 r_0^\xi \bar{R} + \tau \gamma_0^\xi - \bar{p}_0 \delta_0^\xi - \alpha_\xi. \quad (3.40)$$

If all terms except the first in Ξ vanish, then the local melt fraction $\xi = 0$ for $\theta \leq \theta_T$ and ξ increases with θ for $\theta > \theta_T$. Solidification is possible (i.e., $d\xi < 0$) in that case if θ subsequently decreases. However, (3.37) with $\bar{\xi} \rightarrow \xi$ ensures non-negative dissipation $\varsigma d\xi \geq 0$ only when $d\xi \geq 0$, with $\varsigma < 0 \Rightarrow d\xi = 0$. The case $d\xi < 0$ when $\varsigma > 0$ is not ruled out. In calculations, non-negative dissipation can be enforced by the constraint $d\xi = \langle d\bar{\xi} \rangle$. Solidification is accordingly eliminated. A different ODE involving some sign changes to (3.37) is needed to model dissipative, metastable reverse transitions (i.e., solidification) [64, 65, 86].

3.6 Temperature

Substituting (3.22), (3.31), and (3.32) into (3.23), for $\phi \leq 1$ and $\gamma_0^\xi = 0$ as invoked in §4–§6, gives

$$\dot{\theta} = \frac{\beta_0}{c_V} \left[1 - \frac{\alpha_0}{\chi_0} H(W^P - W^\phi) \right] \chi_0 g_0 \omega \mathbf{t}^\xi \left(1 + \frac{\gamma}{\gamma_0} \right)^n \left(\frac{\theta}{\theta_0} \right)^\nu \left(\frac{\dot{\gamma}}{\dot{\gamma}_0} \right)^m \dot{\gamma} - \frac{[\mu_0 r_0^\xi \bar{R} - h_T - \bar{p}_0 \delta_0^\xi] d\mathbf{t}^\xi}{c_V d\xi} \dot{\xi}. \quad (3.41)$$

This nonlinear differential equation must generally be solved numerically for $\theta(\gamma, y)$ at each $y \in [0, h]$, in conjunction with (3.33) for $\phi(\gamma, y)$, (3.36) for $\xi(\gamma, y)$, and (3.25) for $\bar{R}(\gamma, y)$. If functional forms $\phi(\gamma(y, t), y)$, $\xi(\gamma(y, t), y)$, and $\bar{R}(\gamma(y, t), y)$ exist, then at fixed y (3.41) can be written

$$\frac{d\theta}{d\gamma} = \frac{\beta_0}{c_V} \left[1 - \frac{\alpha_0}{\chi_0} H(W^P - W^\phi) \right] \chi_0 g_0 \omega \mathbf{t}^\xi \left(1 + \frac{\gamma}{\gamma_0} \right)^n \left(\frac{\theta}{\theta_0} \right)^\nu \left(\frac{\dot{\gamma}}{\dot{\gamma}_0} \right)^m - \frac{[\mu_0 r_0^\xi \bar{R} - h_T - \bar{p}_0 \delta_0^\xi] d\mathbf{t}^\xi d\xi}{c_V d\xi d\gamma}. \quad (3.42)$$

This equation likewise must be solved numerically. But if melting never occurs, $\xi = 0 \Rightarrow \mathbf{t}^\xi = 1$, and, given function $\phi(\gamma)$ at y , (3.42) can be separated and integrated from $\theta(y, 0) = \theta_i(y)$ as

$$\begin{aligned} \theta^{-\nu} d\theta &= \left\{ \frac{\beta_0}{c_V \theta_0^\nu} \left[1 - (\alpha_0/\chi_0) H(W^P - W^\phi) \right] \chi_0 g_0 \omega \left(1 + \frac{\gamma}{\gamma_0} \right)^n \left(\frac{\dot{\gamma}}{\dot{\gamma}_0} \right)^m \right\} d\gamma \Rightarrow \\ \theta(\gamma) &= \left[\theta_i^{1-\nu} + \frac{(1-\nu)\beta_0 \chi_0 g_0 \gamma_0}{(1+n)c_V \theta_0^\nu} \left(\frac{\dot{\gamma}}{\dot{\gamma}_0} \right)^m \left\{ \left(1 + \frac{\gamma_f}{\gamma_0} \right)^{1+n} - 1 \right\} \right. \\ &\quad \left. + \frac{(1-\nu)(\chi_0 - \alpha_0)\beta_0 g_0}{c_V \theta_0^\nu} \left(\frac{\dot{\gamma}}{\dot{\gamma}_0} \right)^m \int_{\gamma_f}^{\gamma} \omega(\phi(\hat{\gamma})) \left(1 + \frac{\hat{\gamma}}{\gamma_0} \right)^n d\hat{\gamma} \right]^{\frac{1}{1-\nu}}, \quad (\text{if no melting}). \quad (3.43) \end{aligned}$$

The solution for $\theta(\gamma)$ in (3.43) presumes fracture occurs during the strain history, that is, $\gamma \geq \gamma_f$. If $\gamma < \gamma_f$, (3.43) holds with $\gamma_f \rightarrow \gamma$ such that the integral embedded on the right involving ω vanishes. In the latter case, the analytical solution matches Ref. [8] in the absence of phase transformations.

4 Localization and numerical methods

4.1 Failure modes

Three different shear failure criteria are defined:

- **Shear banding.** This is the L_∞ localization definition of Molinari and Clifton [11, 12, 14] also used in Ref. [8]. With reference to the last of (3.20), failure by localization of shear strain $\gamma(Y, t)$ occurs at material point B with $Y = Y_B$ and time t_c when $\gamma(Y_B, t)/\gamma(Y_A, t) = \gamma_B(t)/\gamma_A(t) \rightarrow \infty$ with increasing time $t \geq t_c$ for every point A with $Y_A \neq Y_B$. If $\dot{\gamma}$ remains bounded, $\tau \rightarrow 0$ as $\gamma_B \rightarrow \infty$, meaning shear stress vanishes at some time $t > t_c$.

- **Shear fracture.** As in phase-field and continuum damage mechanics, shear fracture occurs when order parameter $\phi \rightarrow 1$. In the present analysis, shear fracture will generally occur earliest at a point Y_B due to an initial defect. If $\omega_1 = 0$ in (3.29), then $\tau \rightarrow 0$ upon shear fracture. If $\omega_1 > 0$, some (small) fraction of strength can be maintained, depending on whether shear banding or melting take place concurrently.
- **Melting.** Failure by melting occurs when order parameter $\xi \rightarrow 1$. In the present analysis, melting will tend to occur first where temperature rise is largest, which correlates with high-strain regions triggered by initial defects (e.g., at point Y_B). In (3.39), $\tau \rightarrow 0$ as $\xi \rightarrow 1$ if $\iota_1^\xi = 0$. But if $\iota_1^\xi > 0$, then some fraction of strength can be maintained depending on whether shear banding or shear fracture occur simultaneously.

Shear band failure, by definition, requires infinite strain at Y_B . Shear fracture and melting may or may not ensue infinite strain, depending on assumptions and parameters entering their governing equations. For example, $\gamma_B \rightarrow \infty$ is required for $\phi \rightarrow 1$ in (3.35) if $\omega_1 = 0$, but not if $\omega_1 > 0$. The model in (3.40) requires $\gamma_B \rightarrow \infty$ to approach infinite θ or \bar{R} for $\xi \rightarrow 1$. If infinite strains are not required, fracture or melt failure can precede shear band failure. Depending on constitutive parameters for viscoplasticity, fracture, and melting, one or more failure modes may be impossible. Using a different theory, phase-field simulations [31] suggested a tendency for fracture to dominate shear band instability and failure in steel under dynamic torsion as applied strain rate increases.

First consider failure by shear banding. Equality $\tau_A^{1/m} = \tau_B^{1/m}$ of (3.20) is integrated to any time $t = t_a > 0$, with integration limits $\gamma_A = \gamma(Y_A, t_a)$ and $\gamma_B = \gamma(Y_B, t_a)$, initial conditions $\chi_{0A} = \chi_0(Y_A)$, $\chi_{0B} = \chi_0(Y_B)$, and flow stress function (3.28). Then changing variables and dividing by $g_0^{1/m}/\dot{\gamma}_0$,

$$\begin{aligned}
& \int_0^{t_a} [g_0 \chi_{0A} \omega(\phi(\gamma(Y_A, t))) \iota^\xi(\xi(\gamma(Y_A, t)))]^{1/m} [1 + \gamma(Y_A, t)/\gamma_0]^{n/m} [\theta(\gamma(Y_A, t))/\theta_0]^{v/m} \dot{\gamma}_0^{-1} \dot{\gamma}(Y_A, t) dt \\
&= \int_0^{t_a} [g_0 \chi_{0B} \omega(\phi(\gamma(Y_B, t))) \iota^\xi(\xi(\gamma(Y_B, t)))]^{1/m} [1 + \gamma(Y_B, t)/\gamma_0]^{n/m} [\theta(\gamma(Y_B, t))/\theta_0]^{v/m} \dot{\gamma}_0^{-1} \dot{\gamma}(Y_B, t) dt \\
&\Rightarrow \int_0^{\gamma_A} \chi_{0A}^{1/m} \{\omega(\phi(\gamma)) \iota^\xi(\xi(\gamma))\}^{1/m} (1 + \gamma/\gamma_0)^{n/m} [\theta(\gamma)/\theta_0]^{v/m} d\gamma \\
&= \int_0^{\gamma_B} \chi_{0B}^{1/m} \{\omega(\phi(\gamma)) \iota^\xi(\xi(\gamma))\}^{1/m} (1 + \gamma/\gamma_0)^{n/m} [\theta(\gamma)/\theta_0]^{v/m} d\gamma. \tag{4.1}
\end{aligned}$$

Dependence of ξ and ϕ on Y independently of γ is permitted but is not written explicitly in (4.1). If L_∞ localization occurs, $t_a \rightarrow t_c$, $\gamma_B \rightarrow \infty$, and $\gamma_A \rightarrow \gamma_{Ac}$, where $\gamma_{Ac} > 0$ is finite:

$$\begin{aligned}
& \int_0^{\gamma_{Ac}} \chi_{0A}^{1/m} \{\omega(\phi(\gamma)) \iota^\xi(\xi(\gamma))\}^{1/m} (1 + \gamma/\gamma_0)^{n/m} [\theta(\gamma)/\theta_0]^{v/m} d\gamma \\
&= \lim_{\gamma_B \rightarrow \infty} \int_0^{\gamma_B} \chi_{0B}^{1/m} \{\omega(\phi(\gamma)) \iota^\xi(\xi(\gamma))\}^{1/m} (1 + \gamma/\gamma_0)^{n/m} [\theta(\gamma)/\theta_0]^{v/m} d\gamma = \lim_{\gamma_B \rightarrow \infty} \int_0^{\gamma_B} I(\gamma) d\gamma. \tag{4.2}
\end{aligned}$$

As explained in Refs. [11, 12], because γ_{Ac} is finite by definition, the integrals on the left, and thus the right, sides of (4.2) must all be bounded. This means L_∞ localization occurs if and only if $I(\gamma)$ is integrable as $\gamma \rightarrow \infty$. In Refs. [8, 11, 12], bounds on viscoplastic properties n , v , and m

were derived for which L_∞ localization (i.e., shear band failure) is possible. These prior derivations, based on power-law viscoplasticity and analytical solutions for $\theta = \theta(\gamma)$, did not consider shear fracture or melting. In the current setting, three possibilities emerge:

1. Order parameters ϕ or ξ evolve with γ as $\gamma \rightarrow \infty$. No definite criteria for the possibility of L_∞ localization are derived since θ , ω , and ι^ξ depend on γ in forms not known analytically.
2. Either (or both of) $\phi \rightarrow 1$ or $\xi \rightarrow 1$ occurs at finite γ_B with $\omega_1 = 0$ or $\iota_1^\xi = 0$. In this case, fracture or melt failure precedes shear band failure; the latter never occurs since γ_B is finite.
3. Both ϕ and ξ attain fixed terminal values less than unity, or attain unit values with $\omega_1 > 0$ and $\iota_1^\xi > 0$, at finite γ_B . In this case, since ϕ and ξ cease to evolve, they do not influence behavior of $\theta(\gamma)$ in (3.43) as $\gamma \rightarrow \infty$, and ω and ι^ϕ become nonzero constants. Thus, the original criterion for the possibility of L_∞ failure applies (see derivations in Refs. [8, 11, 12]):

$$v + n + (1 - v)m < 0, \quad [\forall m > 0, v < 1], \quad (4.3)$$

most valid for $m \ll 1$. A Newtonian fluid is recovered for $n = 0$ and $m = 1$, whereby (4.3) is violated. A slightly different analysis of non-hardening ($n = 0$) materials [12] gives the localization criterion $v + m < 0$, also violated for any Newtonian fluid with $v \geq -1$. Hence, Newtonian viscosity of molten material must be omitted for L_∞ failure, as done herein.

Next consider failure by fracture in the context of (3.35). If $\omega_1 > 0$, shear fracture is possible at finite γ , necessarily preceding failure by shear banding or melting. However, as some strength is maintained when $\omega_1 > 0$, residual material can still fail by melting, and possibly, shear banding. If $\omega_1 = 0$, then $\gamma \rightarrow \infty \Rightarrow W_f^P \rightarrow \infty \Rightarrow \phi \rightarrow 1$. Failure by shear fracture, melting, and potential shear banding can take place concurrently as $\gamma \rightarrow \infty$, but criterion (4.3) does not necessarily hold.

Lastly consider failure by melting in the context of heuristic model (3.40) with $\gamma_0^\xi = 0$, $h_T > 0$, and $a_\xi = \text{constant}$. Since \bar{R} is non-negative by (3.25), $\theta(\gamma) \rightarrow \infty \Rightarrow \Xi \rightarrow \infty \Rightarrow \xi \rightarrow 1$. It is anticipated, but not proven, that melt failure occurs iff $\gamma \rightarrow \infty$ with $\omega > 0$, meaning complete melting at infinite strain if complete strength loss from fracture has not occurred already. In contrast, if $\omega \rightarrow 0 \Rightarrow \tau \rightarrow 0$ at finite γ , then failure by melting, like failure by shear banding, does not arise, since plastic dissipation supplying a temperature rise ceases and \bar{R} becomes constant after shear fracture. If shear fracture does not occur at finite γ , then simultaneous shear banding, melt failure, and shear fracture are possible as $\gamma \rightarrow \infty$, but (4.3) need not necessarily apply for shear banding.

4.2 Homogeneous solutions

Henceforth, the analysis allows non-uniform $\chi_0 = \chi_0(Y)$ and sets $\theta_i = \theta_0 = \text{constant}$. All other physical properties are constant over Ω_0 . If χ_0 is uniform, L_∞ localization cannot occur: all points Y are indistinguishable so will share the same stress-strain-temperature history. Failure by shear fracture and melting remain possible. These could occur at finite or infinite γ . For homogeneous conditions, the entire slab would fracture or melt simultaneously. Average strain $\bar{\gamma}$ and defect parameter $\bar{\chi}_0$ in the slab, whose average strain rate is $\dot{\bar{\gamma}}$ since $v_0 = \text{constant}$, with $\hat{y} = (J^E)^{1/3}Y$, are

$$\bar{\gamma}(t) = \frac{v_0 t}{h_0} = \frac{1}{h_0} \int_0^{h_0} \gamma(Y(\hat{y})) d\hat{y}, \quad \bar{\chi}_0 = 1 - \delta \bar{\chi}_0 = \frac{1}{h_0} \int_0^{h_0} \chi_0(Y(\hat{y})) d\hat{y}. \quad (4.4)$$

Factor $(J^E)^{1/3}$ accounts for h_0 being the coordinate of the top of the slab after application of p_0 in Fig. 1 and kinematic ansatz (3.5)–(3.7). If $p_0 = 0$, then $\hat{y} = Y$.

For homogeneous conditions, stress from (3.28) is, at fixed p_0 , $\dot{\gamma} = \dot{\bar{\gamma}}$, and $\chi_0 = \bar{\chi}_0$,

$$\bar{\tau}(\bar{\gamma}, \xi(\bar{\gamma}), \phi(\bar{\gamma}), \theta(\bar{\gamma})) = g_0 \bar{\chi}_0 t^\xi (\xi(\bar{\gamma})) \omega(\phi(\bar{\gamma})) (1 + \bar{\gamma}/\gamma_0)^n [\theta(\bar{\gamma})/\theta_0]^v [\dot{\bar{\gamma}}/\dot{\gamma}_0]^m. \quad (4.5)$$

Order parameters and temperature are uniform, but functions $\phi(\gamma)$, $\xi(\gamma)$, and $\theta(\gamma)$ are not known analytically except in degenerate cases. Rather, (3.33), (3.37), and (3.42) comprise a set of three coupled ODEs to be integrated numerically, concurrently with (4.5), over the strain history $\gamma(t)$:

$$d\phi/d\gamma = \mathcal{F}_\phi(\gamma, \xi, \phi, \theta), \quad d\xi/d\gamma = \mathcal{F}_\xi(\gamma, \xi, \phi, \theta), \quad d\theta/d\gamma = \mathcal{F}_\theta(\gamma, \xi, \phi, \theta). \quad (4.6)$$

Initial conditions prescribed for (4.6) are $\phi(0) = \xi(0) = \bar{R}_0 = 0$ and $\theta(0) = \theta_0$.

4.3 Localization calculations

Among all possible positions Y in the slab, localization ensues at the earliest possible t_c , at point $Y = Y_B$, for which the rightmost integral in (4.2) is a minimum [11, 12]. Shear band failure, if occurring, commences at $Y_B = \operatorname{argmax}\{\delta\chi_0\}$ where χ_{0B} is a minimum. This follows from the integrand of $\int_0^{t_c} \tau^{1/m} dt$ in (4.1) being non-negative and approaching zero only as $t \rightarrow t_c \Leftrightarrow \gamma_B \rightarrow \infty$ at B . This threshold integral for localization at Y_B drops as χ_{0B} decreases because $\chi_0 > 0$ and $m > 0$. For $m \ll 1$, the localization integral is very sensitive to the perturbation $\delta\chi_0$ [8, 11, 12].

A shear band approaches a singular surface at Y_B across which displacement has a jump discontinuity as $\gamma \rightarrow \infty$. It is assumed that γ and $\dot{\gamma}$ are continuous functions of Y except at singular point(s) Y_B at $t \geq t_c$. In the shear band, from (4.1) and (4.2), $\tau^{1/m}/\dot{\gamma} \rightarrow 0$ at B as $t \rightarrow t_c$. At $t < t_c$, since $\gamma(Y)$ is continuous, γ_A at at least one location Y_A (that can in principle vary with t) must match $\bar{\gamma} = v_0 t/h_0$. If this Y_A is time-independent, then $\dot{\gamma}_A = \dot{\bar{\gamma}} = v_0/h_0$ identically. Stress exactly from (3.28) in that scenario, otherwise approximated by (3.31) at each Y_A , is given by (4.5) for $t < t_c$. From (3.20), this value of τ is equally valid for the entire Y -domain for $t < t_c$. Equations (4.6) are likewise valid to the same order of approximation for $t < t_c$, with estimate $\chi_0 \approx \bar{\chi}_0$ in \mathcal{F}_ξ and \mathcal{F}_θ [8, 12, 14], noting \mathcal{F}_ϕ does not depend on χ_0 . With these assumptions, $\dot{\gamma}$ affects the solution only through τ , and since τ is uniform over Ω_0 , it follows that θ , ϕ , and ξ are suitably approximate functions only of γ at each point Y , for given loading and initial conditions v_0 , p_0 , and $\bar{\chi}_0$.

Computation of average localization strain $\bar{\gamma}_c$ proceeds as in Ref. [8]. Point Y_B is that for which $Y_B = \operatorname{argmax}\{\delta\chi_0(Y)\} = \operatorname{argmin}\{\chi_0(Y)\}$. A numerical value of the right integral in (4.2) is found as $\gamma_B \rightarrow \infty$. This integral converges (diverges) if L_∞ localization is possible (impossible). If converged, the left of (4.2) is set to this value at all Y_A where $\chi_{0A} > \chi_{0B}$ and solved for $\gamma_{Ac}(Y)$ at each $Y \neq Y_B$. Critical strain $\bar{\gamma}_c$ is lastly found by integrating $\gamma = \gamma_{Ac}(Y)$ over Y in (4.4). Letting $I(\gamma(Y))$ be any integrand in (4.2) and setting $\gamma_{Ac}(Y) = 0$ at $Y = Y_B$ to exclude singularities [11, 12],

$$\gamma_{Ac} = \operatorname{arg} 0 \left[\int_0^{\gamma_A} I(\gamma(Y_A)) d\gamma - \lim_{\gamma_B \rightarrow \infty} \int_0^{\gamma_B} I(\gamma(Y_B)) d\gamma \right], \quad \bar{\gamma}_c = \frac{1}{h_0} \int_0^{h_0} \gamma_{Ac}(Y(\hat{y})) d\hat{y}. \quad (4.7)$$

Numerical iteration is used to solve the first of (4.7), and numerical integration to solve the second of (4.7). The localization threshold integral on the right of (4.2), and thus $\bar{\gamma}_c$ and t_c , are affected by

transients in ϕ and ξ ; how so depends on properties and is not obvious from inspection. As strain in the vicinity of the band accommodates more of the average, γ drops elsewhere for the same $\bar{\gamma}$.

Previous calculations [8, 11, 12] did not seek to model degradation and failure within the adiabatic shear band. Therein, $\bar{\gamma} = \bar{\gamma}_c$ for $t \geq t_c$, and the drop to zero stress upon localization was modeled abruptly (e.g., $\bar{\tau} = 0$ for $t > t_c$). A different approach is taken in the present work, similar to Refs. [27, 28, 45]. These studies likewise used plastic work-threshold based damage models for adiabatic shear failure to capture gradual post-localization stress decay as witnessed in torsion experiments on iron and steels (e.g., [5, 6, 58]). Recall $\bar{\gamma}_c$ of (4.7) is the average strain in the slab that numerically excludes the contribution of the core of the fully formed shear band at Y_B : this core is infinitesimally wide but supports infinite shear strain $\gamma_{Bc} \rightarrow \infty$. The latter's contribution, from a discrete zone wherein shear fracture tends to concentrate, is represented by effective jump in shear displacement $\Delta_\phi(t) \geq 0$ that can be formally derived using Gauss's theorem [74, 87, 88]:

$$\bar{\gamma}(t) = \bar{\gamma}_c + \Delta_\phi(t)/h_0, \quad [\forall t \geq t_c; \Delta_\phi(t) = 0 \forall t \leq t_c]. \quad (4.8)$$

Post-localization shear displacement jump Δ_ϕ need not be calculated explicitly, but it can be using $\bar{\gamma} = \nu_0 t/h_0$ and $\bar{\gamma}_c$ from (4.7). The average strain $\bar{\gamma}$ in (4.8) is identified with $\bar{\gamma}$ in (4.5) to calculate stress $\bar{\tau}$ for $t > t_c \leftrightarrow \bar{\gamma} > \bar{\gamma}_c$ and $\bar{\chi}_0 < 1$. Physical consistency of this post-localization stress calculation requires that $\bar{\gamma}_c$ match the applied strain needed for ductile shear fracture to initiate under macroscopically homogeneous deformation, as in (4.5) of §4.2. Only the average stress decay is continuously depicted for the time history $t > t_c$. Transients of local state variable fields γ , θ , ϕ , and ξ are not modeled for the entire time history $t > t_c$. However, the limit analysis does produce contours $(\cdot)_c$ representing state variables at the final, failed material state as $\bar{\tau} \rightarrow 0$ and $t \gg t_c$.

In some demonstrative calculations of §5 and §6, ductile fracture is suppressed by setting threshold $W_0^\phi \rightarrow \infty$. In those calculations, $\Delta_\phi = 0$ is imposed and local fields remain static for any $t > t_c$. For melt failure, this is consistent with neglecting viscosity of the liquid. For shear banding without resolution of ductile degradation, the predicted abrupt post-localization load drop is consistent with prior numerical implementations of the L_∞ criterion [8, 11, 12].

Defect $\tilde{\phi}_0(Y) = \delta\chi_0(Y)$, with a distribution assigned as in Refs. [8, 73], instigates localization at a single point Y_B at the midsection of the slab Ω_0 in Fig. 1. Recall \hat{y} is the coordinate at $t = 0^+$ after application of p_0 but preceding shear by $\gamma(t)$. With h_0 identified in Fig. 1, define \tilde{y} having its coordinate origin at the midpoint of Ω_0 : $\hat{y} = \frac{1}{2}h_0 \leftrightarrow \tilde{y} = 0$. The initial defect distribution (i.e., yield strength perturbation) of intensity ε_0 and width λ_0 is prescribed in dimensionless form as [8, 73]

$$\begin{aligned} \delta\chi_0(\tilde{y}(Y)) &= \varepsilon_0 \exp[-(2\tilde{y}/\lambda_0)^2], \quad [0 < \lambda_0 \leq 1, \varepsilon_0 \geq 0]; \\ \tilde{y}(Y) &= (2/h_0)[\hat{y}(Y) - h_0/2] = (2/h_0)[(J^E(p_0))^{1/3}Y - h_0/2] \in [-1, 1]; \\ \delta\bar{\chi}_0 &= 1 - \bar{\chi}_0 = \frac{1}{2} \int_{-1}^1 \delta\chi_0 d\tilde{y} = \frac{\sqrt{\pi}}{4} \varepsilon_0 \lambda_0 \operatorname{erf}\left[\frac{2}{\lambda_0}\right] \approx 0.4431 \varepsilon_0 \lambda_0. \end{aligned} \quad (4.9)$$

In calculations, γ and y domains are discretized into dimensionless increments $d\gamma$ and $d\tilde{y}$. Taking $d\gamma, d\tilde{y} \lesssim 10^{-4}$ is generally sufficient for $\bar{\gamma}_c$ independent of grid size. With numerical integration limited by machine precision and an infinite number of increments $d\gamma$ impossible, a large enough upper bound on γ_B is consistently used in (4.7) to enable respectable convergence of $\int_0^{\gamma_B} I(\gamma)d\gamma$

toward a constant value if enabled by properties (e.g., (4.3)) and loading conditions. Convergence quickens with fracture or melting: $(t^\xi \omega)^{1/m} \rightarrow 0$ rapidly with γ as $\phi(\gamma) \rightarrow 1$ or $\xi(\gamma) \rightarrow 1$ for $m \ll 1$. In such cases, if failure by shear fracture or melting occurs, (4.7) is still used with singular point Y_B excluded from $\tilde{\gamma}_c$. Infinite strain remains possible at Y_B if material has null strength there.

Numerical results include contours of γ_c , θ_c , ϕ_c , and ξ_c , where subscript $(\cdot)_c$ denotes a quantity as $t \gg t_c$ and $\bar{\tau} \rightarrow 0$. Contours are restricted to dimensionless \tilde{y} -space. They enable comparison of dimensionless widths of high-strain, high-temperature zones centered on singular bands at $\tilde{y} = 0$. Absolute zone widths scale linearly with h_0 if $t_0 = h_0/\nu_0$, ε_0 , and λ_0 are all constants. Minimum widths tend to zero as $h_0 \rightarrow 0$ at fixed λ_0 since gradient regularization, conduction, and inertia are not modeled. To account for regularizing physics and predict absolute shear band widths, more sophisticated numerical methods (e.g., finite difference [21] or finite element [30]) are required.

5 Application to steel

5.1 Properties and parameters

Behavior of a high-strength, low C, Ni-Cr steel (i.e., a type of RHA steel) is analyzed. Mechanical properties follow from experimental studies of the 1970s-1990s [89–93], and for viscoplastic response, model calibrations to experimental data [8, 94]. A typical composition [89, 92] has 0.22 wt.% C, 1.06 wt.% Cr, and 3.15 wt.% Ni, with other trace elements. Material properties and parameters are listed in Table 1. Most properties, and most viscoplastic parameters, are repeated from Ref. [8] where original sources and calibrations can be found. Exceptions are static yield strength g_0 and rate sensitivity m . Values in Refs. [8, 94] provided a best-fit to dynamic compression data optimized for strain rates of $10^4/s$. Experiments modeled in the current work [6] consider a Ni-Cr steel of RHA type, but at lower average rates (e.g., $\dot{\gamma} \approx 3200/s$) and for which a lower flow stress was observed than is predicted via past values $g_0 = 0.693$ GPa and $m = 0.065$. Iron and steels show increasing m for strain rates exceeding around $10^3/s$ due to influences of phonon drag and relativistic mechanisms at very high rates [17, 63, 77, 95, 96]. Logically, m is reduced to better represent rates $\lesssim 10^4/s$; then, g_0 is calibrated to match the experimental torsion data [6] for $\tilde{\gamma} < \tilde{\gamma}_c$.

Like pure Fe, the α , ε , and γ phases of this steel are BCC, HCP, and FCC. At $p = 0$ and $\theta_0 = 300$ K, material is fully of α phase. Near θ_0 , $\alpha \rightarrow \varepsilon$ transformation occurs at $p \approx 13$ GPa, and near zero pressure, $\alpha \rightarrow \gamma$ transformation occurs at $\theta \approx 1000$ K (see Ref. [8] and works cited therein). The present treatment is restricted to $p_0 < 13$ GPa, but shear-induced $\alpha \rightarrow \varepsilon$ transformations, though not reported in known experiments on RHA, might be possible since they have been inferred for Fe [97]. Evidence of the $\alpha \rightarrow \gamma$ transition within shear bands has been noted in some experiments [3, 98], but not others [6, 92]. To keep the analysis and interpretation of results tractable, $\alpha \rightarrow \varepsilon/\gamma$ transitions are not modeled herein. If solid-solid transformations do occur, the analysis amounts to assigning each solid phase the same properties and ignoring any dissipation from transformations.

For localization calculations, λ_0 follows from Ref. [8]. Effects of the initial defect width in (4.9) are explored in §5.2 by two choices $\lambda_0 = 0.5$ and $\lambda_0 = 1.0$. In Refs. [8, 11, 12], ranges of perturbation intensity spanning $\varepsilon_0 \in [10^{-6}, 10^{-1}]$ were considered in parametric calculations on steels and Fe. Therein, $\tilde{\gamma}_c$ decreased approximately linearly with $\log_{10} \varepsilon_0$. In Table 1, $\varepsilon_0 =$

10^{-3} , intermediate among prior cited values, is suitable in §5.2 for matching $\bar{\gamma}_c$ to average shear at localization from experiment [6] when $\lambda_0 = 0.5$. However, as also shown in §5.2, ε_0 is not always a free parameter: ε_0 , λ_0 , W_0^ϕ , and $\bar{\gamma}_c$ are not all independent. In (4.3), $\nu + n + (1 - \nu)m = -0.233 < 0$, so shear band failure is possible for this steel, at least in the absence of melting or fracture.

New parameters not repeated from Ref. [8] are those for the shear fracture model of §3.4 and the melting model of §3.5. For dynamic shear fracture, the simplest physically admissible choices entering (2.10), (3.29), and parameters consistent with experimental data [6] modeled in §5.2 are assumed. These include $f_\phi = \phi$, $\omega_1 = 0$, $k = 1$, $\iota^\phi = 1 - \phi$, and $\gamma_0^\phi = 0$ as in example (3.35). The latter assumes isotropic ductile damage (e.g., spherical voids); detailed microscopy data would be needed to justify a nonzero value. The presently consulted data [6] do not allow independent calibration of γ_0^ϕ and E_C ; setting the former to zero is the simplest choice. The value $W_0^\phi = 450$ MPa is taken verbatim from Ref. [27] on RHA steel, with the caveat that values ranging from 20 to 350 MPa have been used elsewhere for various structural steels [33, 35]. Phase-field studies [29, 30, 33, 35] consistently assign 10% of the plastic work to energy consumed by fracture, giving $\alpha_0\beta_0 = 0.1$ in Table 1. Cohesive energy E_C is unknown a priori for the specific steel of present study; the value $E_C = 25$ MPa in Table 1 is calibrated in §5.2 to the post-localization stress-strain data of Ref. [6]. Values ranging anywhere from 10 to 1600 MPa can be inferred from experimental and phase-field studies on other high-strength steels [4, 29, 30, 33, 35]. Induced porosity at fracture quantified by δ_0^ϕ is difficult to quantify precisely for dynamic shear, but voids and cracks have been observed inside shear bands in experiments on steels [3, 4, 6]. A representative value of 0.05 from Ref. [65] on Fe and other steels is used here. With this choice and the value of E_C in Table 1, tensile pressure that would induce rupture is $-p_0 \approx E_C/\delta_0^\xi = 0.5$ GPa. The corresponding uniaxial tensile stress would be ≈ 1.5 GPa. For reference, the static ultimate tensile strength of RHA steel ranges from 0.8 to 1.2 GPa [7, 89], and spall strengths of Fe and steels range from 0.7 to 3.7 GPa [99].

For melting, $\xi \rightarrow \bar{\xi}$, $\gamma_0^\xi = 0$, and (3.39) is used. Metastable equilibrium, $t_R^\xi \dot{\gamma} \ll 1$, is justified by suitability of shock-wave experiments that complete at timescales on the order of μ s to determine melting curves of Fe [100, 101]. Omission of γ_0^ξ is the usual assumption [54, 55], satisfactory in the limit of sharp interfaces [53, 102]. A nonzero value could be important for modeling nanoscale physics in a regularized phase-field theory [53], but calibration to nm-scale data from experiments or atomic simulations is needed. The equilibrium melt temperature at ambient pressure, θ_T , is around 1800 K in Fe [103] and the present class of steels [93, 94]. Unknown for the current Ni-Cr steel, values of h_T and δ_0^ξ for Fe [103] are used as a substitute. The model can be considered reasonably accurate only for $p_0 \lesssim 10$ GPa since a near-linear dependence of melt start temperature on pressure is predicted by (3.39). At higher p_0 , experiments and atomic simulation data show highly nonlinear melt curves for Fe [100, 101]. Such data also show mixed-phase regions where liquid and solid coexist at a given θ and p_0 . The width of the mixed-phase region, and dissipation from melting, are controlled by β_ξ , for which precise values are unknown. Assumed in Table 1 are two choices for β_ξ : one, for “fast melting” with $\beta_\xi = 0.18$ GPa, one for “slow melting” with $\beta_\xi = 1.21$ GPa. For the former, under purely thermal loading, $\xi = 0.99$ at $\frac{\theta}{\theta_T} = 1.2$. For the latter, $\xi = 0.5$ at $\frac{\theta}{\theta_T} = 1.2$. Redundant in the present setting, null values $a_\xi = 0$ and $\iota_1^\xi = 0$ are assigned. Admissible minimum and maximum values of r_0^ξ are explored in calculations: $r_0^\xi = 0$ and $r_0^\xi = 1$.

Table 1. Properties or model parameters for Ni-Cr steel, $\theta_0 = 300$ K

Parameter [units]	Definition	Value	Parameter [units]	Definition	Value
ρ_0 [g/cm ³]	ambient mass density	7.84	c_V [MPa/K]	specific heat	3.48
B_0 [GPa]	isothermal bulk modulus	163	h_T [GPa]	latent heat of fusion	2.09
B'_0 [-]	pressure derivative of B	5.29	δ_0^ξ [-]	melt volume change	0.052
μ_0 [GPa]	elastic shear modulus	80	θ_T [K]	equilibrium melt	1800
μ'/μ_0 [1/GPa]	pressure dependence of μ	0.024	β_ξ [GPa]	melt kinetic barrier	0.18, 1.21
g_0 [GPa]	initial yield strength	0.40	W_0^ϕ [GPa]	damage start threshold	0.45
γ_0 [-]	reference plastic strain	0.01	α_0 [-]	fracture energy ratio	0.125
$\dot{\gamma}_0$ [1/s]	reference strain rate	1.0	E_C [GPa]	fracture cohesive energy	0.025
n [-]	strain hardening exponent	0.05	δ_0^ϕ [-]	porosity at failure	0.05
m [-]	strain rate sensitivity	0.035	ω_1 [-]	residual strength factor	10^{-5}
ν [-]	thermal softening	-0.33	ε_0 [-]	nominal defect intensity	10^{-3}
β_0 [-]	Taylor-Quinney factor	0.8	λ_0 [-]	initial defect width	0.5, 1.0

5.2 Numerical results

Outcomes of calculations invoking methods of §4.2 and §4.3, with baseline properties of Ni-Cr steel in Table 1, are reported next. Results in §5.2 consider only null external pressure (i.e., $p_0 = 0 \Leftrightarrow J^E = 1$). Results are compared with dynamic torsion data of Ref. [6], specifically data from the experiment on specimen labeled “B6”. In that work [6], a torsional split Hopkinson (i.e., Kolsky) bar was used to determine average dynamic shear stress versus shear strain behavior, and local strains and strain rates were calculated by analyzing high-speed photographs taken in-situ on portions of specimens marked beforehand with regularly spaced grids. Data for six specimens of 2-mm length were reported, but local strain distributions were only shown for B6 (hence the reason for modeling that particular sample). Among the six samples, average wall thickness varied by $\approx 10\%$, mean strain rates varied up to a factor of two, and localization was observed in four of the six experiments. Among those four, estimated times and strains at localization onset varied by around 50%. As the material is not extremely rate sensitive, test-to-test variations are attributed to different initial defects that could possibly be linked to thickness perturbations [8, 11, 12].

Recall the shearing rate of the present framework is $\dot{\gamma} = 2\dot{\varepsilon}$, where in the absence of dilatation, the true local strain rate is $\dot{\varepsilon} = \dot{\varepsilon}_{xy} = \frac{1}{2}(\partial v_x/\partial y + \partial v_y/\partial x)$. The mean shearing rate ¹ for test B6 is taken as $\dot{\gamma} = 3200$ /s, depicting the average reported by the Hopkinson bar analysis [6]. After localization begins, the mean shear strain rate remains reasonably constant according to the Hopkinson bar analysis, but image analysis suggests it could vary [6]. The former experimental result is used herein; the framework in §4 requires $\dot{\gamma} = \text{constant}$, and further omits inertial effects that would seem more prominent if the average, in addition to local, strain rate fluctuated strongly in time. Total average strain from experiment B6 is converted from a start time $t = 0$ when the

¹The strain measure in Ref. [6] does not appear to be formally defined therein; here, it is interpreted as true strain. If, instead, it is nominal strain (with rotation), then experimental values of γ and $\dot{\gamma}$ quoted herein should be multiplied by $\frac{1}{2}$. Threshold energy W_0^ϕ would be similarly reduced. Forthcoming trends in model predictions should be unchanged, but adiabatic temperature rise would be smaller. The present true-strain interpretation is supported by consistency of the current model and parameters (i.e., Table 1) with the identical value of W_0^ϕ quoted for RHA in Ref. [27].

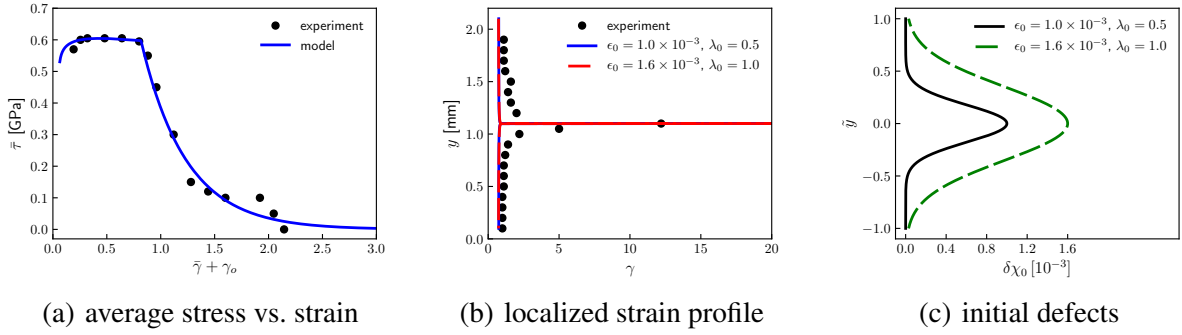


Figure 2. Model results and experimental torsion data [6]: (a) average shear stress $\bar{\tau}$ vs. average shear strain $\bar{\gamma}$ (strain in rigid-plastic model shifted by γ_o to compensate for oscillatory elastic ramp-up in experiments, not shown) (b) localized strain distribution γ , specimen size $h_0 = 2$ mm (c) two initial defect profiles (ϵ_0, λ_0). Experimental points sample continuous (a) or discrete (b) data from Ref. [6].

experimental load-time history provided by the Hopkinson bar begins. During the early part of the test (i.e., first $\approx 20 \mu\text{s}$ [6]), the stress response is overly compliant and highly oscillatory because the sample has neither loaded fully nor achieved equilibrium needed for a (nearly) uniform stress-strain state [104]. Thus, the oscillatory quasi-elastic offset “strain” $\gamma_o = 3200 \times 20 \times 10^{-6} = 0.064$ contributes to the total calculated this way. For comparison of average stress-strain data with results of the rigid-viscoplastic framework of §3 and §4, this offset must equivalently be subtracted from the experimental record or added to the model reference datum, since prior to $20 \mu\text{s}$, the bulk of the sample has not plastically yielded. Early-time and fine-scale oscillations are omitted [28].

Average stress-strain behaviors are compared in Fig. 2(a). The model result is offset by γ_o as it necessarily excludes the oscillatory elastic ramp-up. The rapid load drop corresponding to the onset of localization appears at $\bar{\gamma} = \bar{\gamma}_c = 0.753$. Recall from §5.1 that the model, with prescribed $\epsilon_0 = 10^{-3}$, is able to accurately match the experimental stress-strain record with calibration of only two parameters: (i) initial yield strength g_0 for average stress up to localization and (ii) cohesive energy E_C for the rate of post-localization stress decay. As will be shown in parametric calculations of §6, the stress drop becomes more abrupt as E_C is reduced or as tensile pressure is increased. Localized strain distributions from model ($\gamma = \gamma_c$) and experiment ($t = 613 \mu\text{s}$) are compared in Fig. 2(b). Model results are shifted upward by $\Delta y = 0.1$ mm so that locations of the centers of the shear bands coincide. This is permissible since γ -contours are nearly independent of \tilde{y} for $|\tilde{y}| \gtrsim 0.9$. Local strains are similarly uniform far from the core at $y = 1.1$ mm, but the model does not capture the strain bulge surrounding the core of the band seen in the experiment. Post-localization strain within the modeled band is depicted by a finite displacement jump Δ_ϕ via (4.8) over a zero-width (i.e., singular) surface. In the experimental record, the band is of finite width, but cracks not evident in the data profile were seen around at least some of the perimeter [6]. Discrepancies can be attributed to missing regularization mechanism(s) in the model (e.g., no conduction, inertia, or gradient surface energies) and limits of experimental resolution emphasized in Ref. [6].

The mean stress-strain behavior is the same when a less concentrated initial defect profile is prescribed, but of higher peak intensity, as depicted in Fig. 2(c). The value of $\epsilon_0 = 1.6 \times 10^{-3}$ must

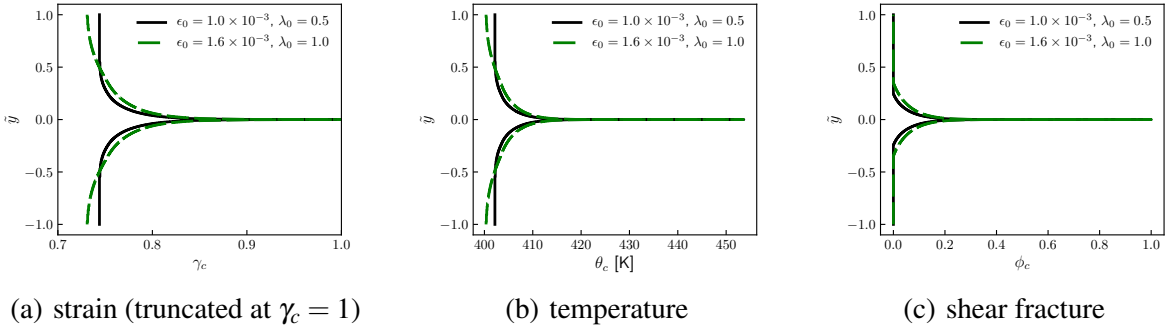


Figure 3. Model results for two initial defect profiles (ϵ_0, λ_0) vs. normalized spatial position \bar{y} : (a) post-localization strain $\bar{\gamma}_c$ (b) temperature θ_c (c) fracture order parameter ϕ_c

be tuned in this case to produce the same value of $\bar{\gamma}_c = 0.753$: a less concentrated defect requires a larger magnitude to induce the same average localization strain.

Effects of the two defect profiles on critical strain, temperature, and ductile fracture parameter distributions are further examined in Figs. 3(a), 3(b), and 3(c). As anticipated, a more diffuse defect produces a wider strain, temperature, and damage distribution away from the infinite-strain band centered at $\bar{y} = 0$ than a narrower initial defect. Maximum temperature θ_c does not reach 500 K in either case. Damage-softening from fracture in the shear band reduces τ to such a low value that plastic working ceases to affect the θ by any pragmatically calculable amount as $\gamma \rightarrow \infty$. Calculations verify temperature rise is insufficient to induce melting, even at the core of the shear band, recalling $\theta_T = 1800$ K. It also appears insufficient to induce $\alpha \rightarrow \gamma$ phase transformation (not enabled in the framework of §2–§4) that occurs at ≈ 1000 K [8, 92]. In the band center, $\phi_c \rightarrow 1$.

Calculations from the full model, fracture suppressed, and both fracture and melting suppressed are considered in Fig. 4. In the full model, labeled “fracture” in Fig. 4(a), melting never occurs; results here are repeated with experimental data from Fig. 2(a). Cases in which fracture is deactivated but melting enabled are denoted “fast melt” and “slow melt” for respective small and large values of kinetic factor β_ξ in Table 1. Different choices of β_ξ and r_0^ξ produce modest differences in the total strain at which localization ensues, beyond which the drop in average stress $\bar{\tau}$ is abrupt per assumptions in §4.3. The largest critical localization strain is predicted when both softening mechanisms (i.e., fracture and melting) are suppressed. Figures 4(b), 4(c), and 4(d) compare predictions of model renditions under homogeneous deformations (i.e., no initial defects: $\epsilon_0 = 0 \leftrightarrow \delta\chi_0 = 0$). When stored energy of cold work fuels melting, then melting begins at $\bar{\gamma} \approx 7.0$. When it does not, melting begins at $\bar{\gamma} \approx 13.3$. Subsequently, melting occurs at a faster rate with respect to $\bar{\gamma}$ for the lower value of β_ξ , as evidenced by the homogeneous melt fraction $\bar{\xi}$ in Fig 4(d). Shear stress decays with increasing $\bar{\xi}$ in Fig. 4(b). Homogeneous temperature $\bar{\theta}$ increases monotonically when melting is suppressed. Since melting consumes energy ($h_T > 0$), the rate of temperature increase is reduced during solid-to-liquid transformation. As seen in Fig. 4(c), for the case of fast melting fueled by energy from dissolution of dislocations, $\bar{\theta}$ can even decrease.

Contours of localized shear strain, temperature, and melt fraction are compared in Fig. 5 for different renditions with fracture suppressed. These correspond to any post-localization time $t > t_c$.

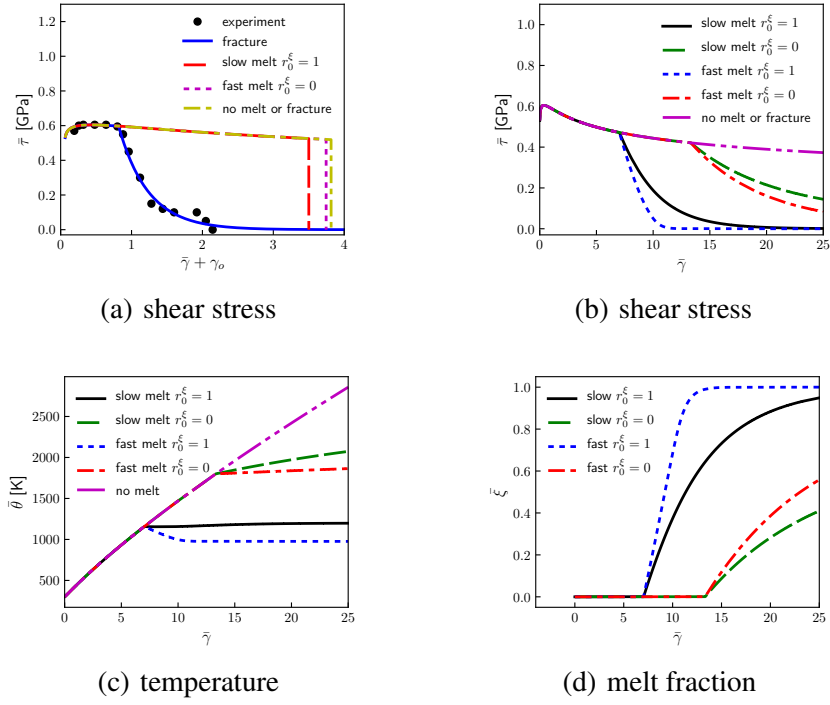


Figure 4. Model results with features activated or suppressed: (a) average shear stress $\bar{\tau}$ vs. average shear strain $\bar{\gamma}$ and experimental torsion data [6]; (b), (c), (d) homogeneous solutions for average shear stress, temperature $\bar{\theta}$, and melt order parameter ξ to extreme shear strain. Slow and fast melt correspond to respective large and small values of β_ξ in Table 1; r_0^ξ is fraction of stored energy of cold work released upon melting.

In Fig. 5(a), local strain γ_c differs very little whether or not melting occurs. Differences are larger among the two different choices of λ_0 . Similar trends are observed for local temperature θ_c in Fig. 5(b), noting that in the core of the shear band at $\bar{\gamma} = 0$, θ_c can exceed 2400 K. Accordingly, as seen in Fig. 5(c), complete melting $\xi_c \rightarrow 1$ is possible in the core. However, temperature and other driving forces (e.g., \bar{R}) are not large enough outside the core to induce appreciable melting. Even partially liquified material is always confined to a very narrow region near the center of the band.

Outcomes of calculations of §5.2 are summarized in Table 2, specifically the average stress $\bar{\tau}_c$ computed at $t = t_c^-$ (i.e., immediately preceding the load drop associated with localization) and the critical average strain from (4.7) as $t \rightarrow t_c$ that, by definition, excludes the contribution Δ_ϕ of (4.8). Since the steel is already thermal softening prior to any localization, lower $\bar{\gamma}_c$ always correlates with larger $\bar{\tau}_c$. A more diffuse defect with larger λ_0 tends to delay localization. For the same initial defect profile, critical localization strain is reduced 80% by ductile shear fracture, but by no more than 12% by melting. Melting never occurs when shear fracture is permitted.

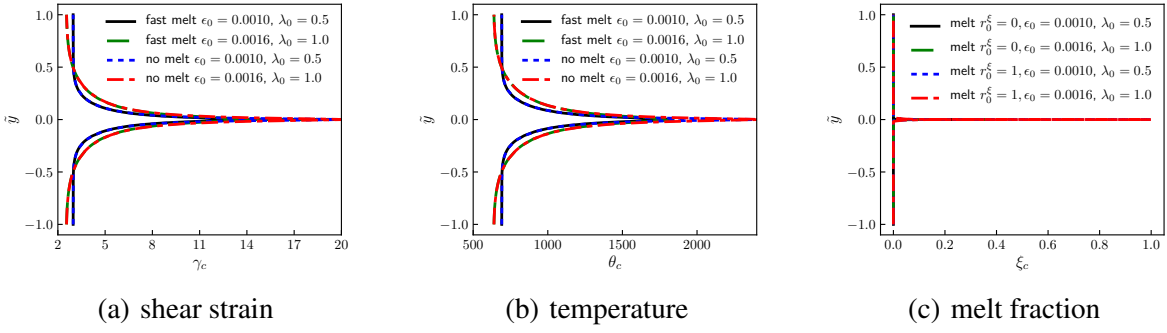


Figure 5. Model results without fracture for two initial defect profiles (ϵ_0, λ_0) vs. normalized spatial position \tilde{y} : (a), (b) strain γ_c , temperature θ_c for $r_0^\xi = 0$ or melt suppressed (c) melt parameter ξ_c for $r_0^\xi = 0, 1$

Table 2. Results summary for high-strength steel, $p_0 = 0$, $\theta_0 = 300$ K, $\dot{\gamma} = 3200/s$

Physics	W_0^ϕ [MPa]	θ_T [K]	ϵ_0 [10^{-3}]	λ_0	β_ξ [GPa]	r_0^ξ	$\bar{\tau}_c$ [MPa]	$\bar{\gamma}_c$
Fracture (full model)	450	1800	1.0	0.5	0.182	1	597	0.753
			1.6	1.0	0.182	1	596	0.753
Melting (no fracture)	∞	1800	1.0	0.5	0.182	1	526	3.432
			1.6	1.0	0.182	1	524	3.515
			1.0	0.5	1.207	1	525	3.437
			1.6	1.0	1.207	1	524	3.521
			1.0	0.5	0.182	0	521	3.681
			1.6	1.0	0.182	0	517	3.874
No fracture or melting	∞	∞	1.0	0.5	0.182	1	519	3.751
			1.6	1.0	0.182	1	515	3.983
			1.0	0.5	1.207	0	521	3.683

6 Parameter variations

Parametric calculations next investigate influences of pressure p_0 and values of W_0^ϕ and E_C entering the ductile fracture theory of §3.4. In all calculations of §6, the defect width $\lambda_0 = 0.5$ per Table 1, but the intensity ϵ_0 can depart from its nominal value of 10^{-3} in Table 1. Quantities labeled by an asterisk $(\cdot)^*$ correspond to nominal property values from Table 1 or to results obtained from calculations using such nominal property values. Pressures are always limited to $|p_0| \leq 5$ GPa.

For calculations reported in Fig. 6, the full model with fracture and possible melting is invoked, but melting never occurs in these particular predictions because fracture always takes place first. As in §5.2, upon shear fracture, stress drops too quickly to enable a large enough temperature rise from stress power to initiate melting, even in the center of the shear band.

Effects of threshold energy W_0^ϕ on critical localization strain $\bar{\gamma}_c$, at fixed E_C , are shown in Fig. 6(a). Three values of applied pressure are considered: zero, 5 GPa compression, and 0.4 GPa tension. Recall from §5.1 that a tensile pressure approaching 0.5 GPa would induce instant cav-

itation and rupture, so larger tensile pressures not modeled here. The magnitude of each initial defect ε_0 needed to achieve the corresponding $\tilde{\gamma}_c$ is shown in Fig. 6(b). Critical average strain increases near linearly with W_0^ϕ but scantily increases (decreases) with compressive (tensile) pressure at fixed W_0^ϕ . Initial defect intensity in Fig. 6(b), in contrast, decreases significantly as tensile stress increases at fixed threshold W_0^ϕ . Furthermore, perturbation strength must decrease to enable larger threshold energy at fixed pressure. Results are physically viable: sensitivity to defects is greater in tension than compression, and threshold energy drops for sharper defects. Threshold energy and initial defects should not be prescribed independently because results show the two are intrinsically coupled. The maximum local temperature in the core of the shear band, among all cases reported in Fig. 6, arises for $W_0^\phi/W_0^{\phi*} = 1.4$ and $p_0 = 5$ GPa, with a post-localization value $\theta = 782$ K. Maximum core temperature increases as W_0^ϕ , E_C , and p_0 increase: threshold energy, cohesive energy, and compressive stress all delay final failure from damage-softening and fracture.

Effects of cohesive energy on defect intensity needed to produce a consistent value of $\tilde{\gamma}_c \approx 0.75$, at fixed $W_0^\phi = W_0^{\phi*}$, are reported in Fig. 6(c). At any value of E_C , a larger defect intensity ε_0 is required in compression, a smaller defect strength in tension. Pressure sensitivity increases for lower values of E_C . At fixed p_0 , a larger E_C requires a more severe defect to engender the same $\tilde{\gamma}_c$, especially under tensile stress. For $p_0 = 5$ GPa, $\tilde{\gamma}_c = 0.757$, whereas $\tilde{\gamma}_c = 0.753$ for $p_0 = 0$ and -0.4 GPa. Cohesive energy and perturbation strength are nearly independent at high compressive pressure. Effects of tensile p_0 and increased E_C are compared with experiment [6] in Fig. 6(d), where ε_0 is prescribed to give $\tilde{\gamma}_c = 0.753$ in all cases shown. Stress decay for $\tilde{\gamma} > \tilde{\gamma}_c$ accelerates under tensile pressure and decelerates when E_C increases.

Barring activation of some catastrophic defect or change in microstructure, adiabatic shear localization should follow, but not precede, instability in a viscoplastic solid [1, 10, 13, 14, 105, 106]. Therefore, as the shear fracture model of §3.4 seeks to represent material degradation within a shear band, a pragmatic lower bound on the threshold plastic work W_0^ϕ , written as \tilde{W}_0^ϕ , corresponds to the plastic work accumulated up to the instability strain $\tilde{\gamma}_c$, that, in homogeneous simple shear, is determined from the condition $d\tau/d\gamma = 0$ under adiabatic conditions at a given initial temperature θ_i , loading rate $\dot{\gamma} = \tilde{\gamma}$, and pressure p_0 . This bound is inherent in prior modeling [28, 45] that used a similar threshold energy density for the onset of damage softening. In the absence of melting, and with $\theta_i = \theta_0$, the power-law flow model of (3.28) with analytical temperature solution of (3.43) ($\gamma_f \rightarrow \gamma$) gives the following implicit solution for minimum localization strain $\tilde{\gamma}_c$ and energy \tilde{W}_c^ϕ :

$$\tilde{\gamma}_c = \arg 0 \left[\frac{n}{vA_c} + \frac{(1 + \frac{\gamma}{\gamma_0})^{1+n}}{1 + A_c(\frac{1-v}{1+n})\{(1 + \frac{\gamma}{\gamma_0})^{1+n} - 1\}} \right], \quad A_c = \frac{\beta_0 \chi_0 g_0 \gamma_0}{c_v \theta_0} \left(\frac{\dot{\gamma}}{\dot{\gamma}_0} \right)^m; \quad (6.1)$$

$$\tilde{W}_0^\phi = \int_0^{\tilde{\gamma}_c} \tau(\gamma, \theta(\gamma)) d\gamma = \frac{c_v \theta_0}{\beta_0} \left[\left\{ 1 + A_c \left(\frac{1-v}{1+n} \right) \left[\left(1 + \frac{\tilde{\gamma}_c}{\gamma_0} \right)^{1+n} - 1 \right] \right\}^{\frac{1}{1-v}} - 1 \right]. \quad (6.2)$$

Parameters from Table 1, $\dot{\gamma} = 3200$ /s, and $p_0 = 0$ give $\tilde{\gamma}_c = 0.372$ and $\tilde{W}_0^\phi = 0.221$ GPa. The former can be compared with Culver's critical strain $\hat{\gamma}_c = -\frac{nc_v \theta}{v\tau}$ (e.g., [7]), where $\hat{\gamma}_c = 0.306$ for calculated peak stress $\tau = 0.605$ GPa and $\theta = 351$ K. Effects of n , v , m , and g_0 on $\tilde{\gamma}_c$ and \tilde{W}_0^ϕ are shown in Fig. 7(a) and Fig. 7(b). Both $\tilde{\gamma}_c$ and \tilde{W}_0^ϕ increase nearly linearly with increasing strain hardening

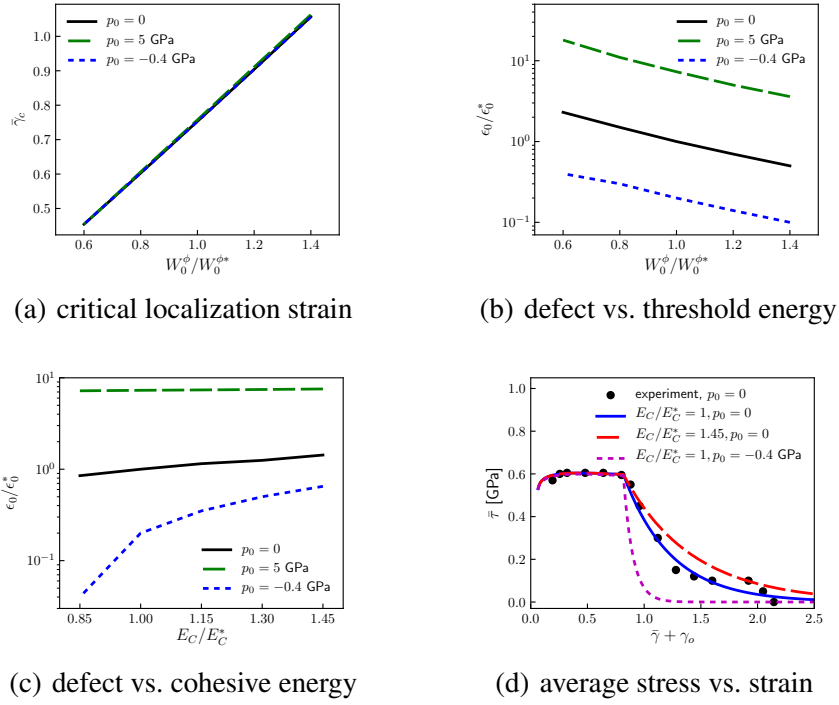


Figure 6. Effects of threshold fracture energy W_0^ϕ , cohesive energy E_C , and pressure p_0 on (a) average strain for localization $\tilde{\gamma}_c$ and (b), (c) initial defect magnitude ϵ_0 consistent with $\tilde{\gamma}_c$ (d) average stress $\bar{\tau}$ vs. strain $\bar{\gamma}$ at $W_0^\phi = W_0^{\phi*}$ with experimental torsion data [6]. Baseline ($W_0^{\phi*}, E_C^*, \epsilon_0^*$) from Table 1.

exponent n . Both decrease nonlinearly with decreasing (more strongly negative) ν , corresponding to more thermal softening. While $\tilde{\gamma}_c$ decreases modestly and nearly linearly with increasing rate sensitivity m , the minimum threshold energy \tilde{W}_0^ϕ is negligibly affected by m . The latter is likewise insensitive to initial static yield strength g_0 , but $\tilde{\gamma}_c$ decreases nonlinearly with increasing g_0 . The latter decrease is a result of proportionally more plastic dissipation and temperature rise, leading to thermal softening that overtakes strain hardening at a lower applied strain.

Implications of varying the equilibrium melt temperature θ_T are also investigated. Parametric calculations reported in Fig. 8(a) study hypothetical cases when fracture is suppressed (i.e., $W_0^\phi \rightarrow \infty$). Here, the defect profile is fixed at nominal values from Table 1: $\epsilon_0 = 10^{-3}$, $\lambda_0 = 0.5$. Influences of compressive or tensile pressure $p_0 = \pm 5$ GPa are considered, where large tensile pressure is admissible since fracture and cavitation are suppressed. Melt temperature θ_T ranges from 450 to 2250 K in Fig. 8(a). In all cases, $\tilde{\gamma}_c$ increases with increasing θ_T at fixed p_0 : loss of shear strength is delayed as the requisite temperature rise for melting increases. In Fig. 8(a), $\tilde{\gamma}_c$ decreases (increases) in tension (compression) at low θ_T , with the opposite trend at high θ_T . The effect of p_0 is greater at high θ_T . Opposing effects ensue: compression resists melting due to $\bar{p}_0 \delta_0^\xi > 0$ in (3.40), but p_0 increases strength via (3.27) and thus dissipative temperature rise that promotes melting.

Lastly, a theoretical case in which fracture and melting take place concurrently is studied. In this case, $\theta_T = 0.225\theta_T^* = 405$ K is low enough that melting begins in the core of the shear band

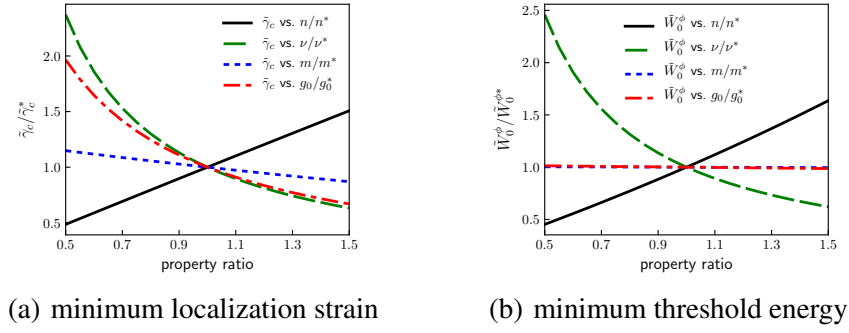


Figure 7. Effects of viscoplastic parameters for strain hardening $n > 0$, thermal softening $v < 0$, rate sensitivity $m > 0$, and yield strength $g_0 > 0$ on minimum localization (i.e., instability) strain $\tilde{\gamma}_c$ and corresponding threshold energy \tilde{W}_0^{ϕ} . Baseline (n^* , v^* , m^* , g_0^*) from Table 1 produce $\tilde{\gamma}_c^* = 0.372$ and $\tilde{W}_0^{\phi^*} = 0.221$ GPa.

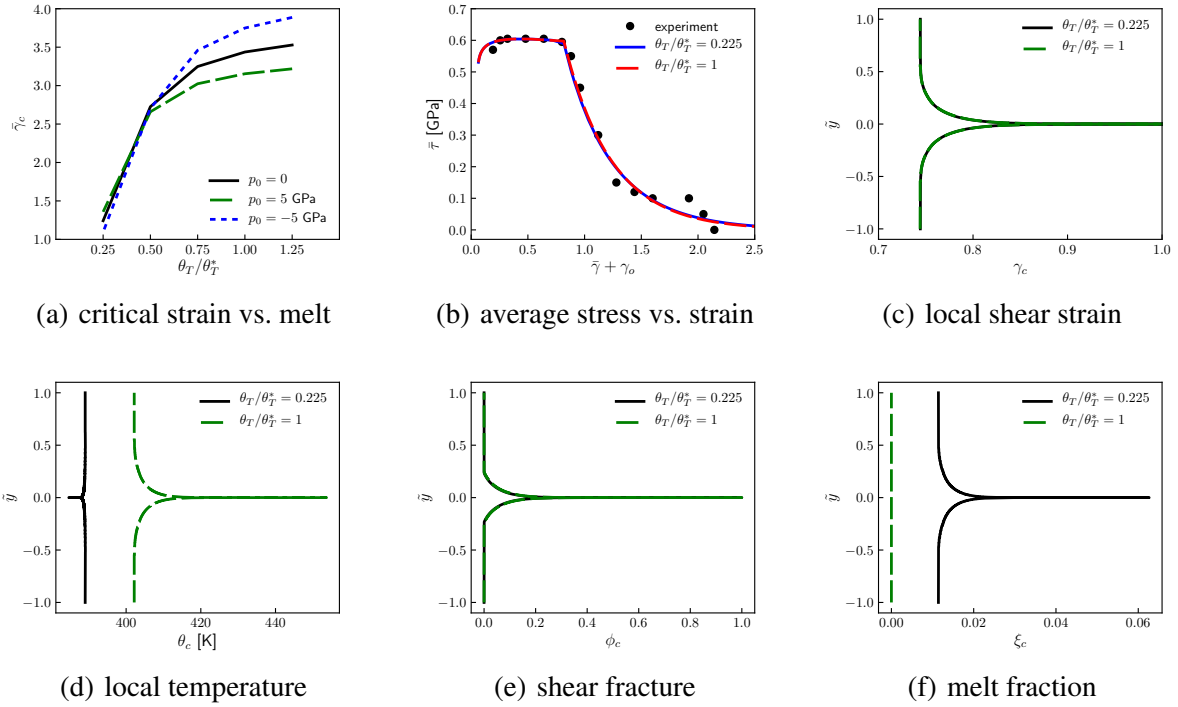


Figure 8. Model results for (a) effects of equilibrium melt temperature θ_T and pressure p_0 on critical localization strain $\tilde{\gamma}_c$ with fracture suppressed (b) average stress vs. strain for reduced and realistic (θ_T^* from Table 1) melt temperatures (fracture enabled) and experimental data [6] (c), (d), (e), (f) post-localization strain γ_c , temperature θ_c , fracture parameter ϕ_c , melt parameter ξ_c for reduced and realistic melt temperatures

even when the fracture model is enabled. Here, all parameters except θ_T and ε_0 are nominal values from Table 1, including the set ($\lambda_0 = 0.5, \beta_\xi = 1.21$ GPa, $r_0^\xi = 1$). The value $\varepsilon_0 = 7 \times 10^{-4}$ is reduced from 10^{-3} so that localization always ensues at $\tilde{\gamma}_c = 0.753$. Average stress-strain behavior

differs little in Fig. 8(b) between the nominal case and reduced melting temperature. Contours of local shear strain γ_c and damage order parameter ϕ_c are also hardly affected by θ_T in Figs. 8(c) and 8(e). The material only partially melts, with nonzero ξ_c limited to a narrow region near the core of the shear band in Fig. 8(f). Temperature θ_c in Fig. 8(d) decreases slightly, relative to surrounding material, in the core where this transition occurs, as thermal energy is consumed by latent heat.

7 Conclusions

An analytical-numerical framework has been advanced to study interplay among adiabatic shear localization, ductile fracture, and melting in viscoplastic solids. The problem studied is adiabatic simple shear with uniform external pressure. Localization initiates when a threshold energy density from cumulative plastic work is attained in the context of a dynamic shear fracture model. Post-localization stress decay is modulated by the cohesive energy (related to the shear-band fracture toughness), with the decay rate increased (decreased) by tensile (compressive) stress. Localization concludes when a band of infinitesimal thickness and infinite shear strain is admitted by solutions to the governing equations. Threshold energy, initial defects (e.g., local strength perturbations), and critical average strain at which localization begins are not independent. Larger threshold energy implies a larger critical strain and a defect of lesser intensity or broader distribution. Sharp intense defects are most deleterious; defect sensitivity increases with tensile pressure. Following the usual convention that instability is a necessary condition for localization, the threshold energy logically increases with strain hardening propensity and decreases with more thermal softening.

The model is exercised using properties for a high-strength steel (i.e., RHA). Calculated results for average stress-strain behavior, including post-localization response, accurately match experimental data from dynamic torsion using a literature value of threshold energy density for steel. Nearly all parameters are obtained from cited research. Calibration is required only for initial yield strength and cohesive energy. The latter's value is within bounds suggested by experiments and prior phase-field studies. Model features and parameters, with fracture enabled, limit accurate calculations to maximum compressive pressures of 5 GPa and tensile pressures under 0.5 GPa.

The framework idealizes the fully formed core of a shear band as a singular region of infinitesimal width and infinite strain. Thus, experimentally measured widths and magnitudes of the band in a continuous sample are necessarily under- and over-predicted, respectively, when experimental profiles do not account for singularities (e.g., shear cracks). Realistic absolute widths cannot be calculated since the analysis includes no material length scale: presently calculated widths are proportional to specimen size for an a priori, normalized initial perturbation profile. To accurately calculate the absolute width, a complete theoretical model with heat conduction, inertia, and phase-field (i.e., damage order-parameter) gradient regularization should be implemented in a numerical scheme with full space-time discretization. The governing equations for such a complete theoretical model have already been included in the theory outlined in §2 of this work, but certain material constants have been zeroed out to allow use of the infinite-strain, singular-point localization criterion pioneered by Molinari and Clifton. High defect sensitivity inherent in this criterion should be reduced in a regularized theoretical-numerical setting: a stronger initial perturbation is expected to be needed to overcome energetic resistance from presently omitted regularization mechanisms.

Calculations suggest that melting is unimportant for shear localization in this steel under dynamic torsion at rates on the order of $10^4/s$. Shear fracture progresses faster than the temperature rise needed for melt initiation. Maximum predicted temperatures in the core of the band are presumably elevated due to omission of thermal diffusion; however, it is possible that the intentionally simple damage model implemented herein omits dissipative structural processes that could competitively increase local temperature. The temperature rise within the shear-softened zone likewise appears insufficient for $\alpha \rightarrow \gamma$ phase transition in this steel. It is not impossible that an $\alpha \rightarrow \epsilon$ transformation could occur, but this transformation has not been confirmed in known experiments on RHA at low pressures (e.g., $p \leq 5$ GPa as studied here). If much higher pressures, or if metals with greater intrinsic resistance to local shear fracture (i.e., much larger threshold or cohesive energies), are considered, then higher temperatures can be attained. Therefore, the present inferences of low importance of melting and phase transitions should not be blindly extrapolated to more extreme pressure conditions, other (e.g., multi-axial) stress-strain histories, or to all kinds of steels.

References

- [1] T.W. Wright. *The Physics and Mathematics of Adiabatic Shear Bands*. Cambridge University Press, Cambridge, 2002.
- [2] N. Yan, Z. Li, Y. Xu, and M.A. Meyers. Shear localization in metallic materials at high strain rates. *Progress in Materials Science*, 119:100755, 2021.
- [3] K. Cho, Y.C. Chi, and J. Duffy. Microscopic observations of adiabatic shear bands in three different steels. *Metallurgical Transactions A*, 21:1161–1175, 1990.
- [4] K. Minnaar and M. Zhou. An analysis of the dynamic shear failure resistance of structural metals. *Journal of the Mechanics and Physics of Solids*, 46:2155–2170, 1998.
- [5] N.A. Fellows and J. Harding. Use of high-speed photography to study localisation during high-strain-rate torsion testing of soft iron. *Materials Science and Engineering A*, 298:90–99, 2001.
- [6] N.A. Fellows and J. Harding. Localization of plastic deformation during high strain rate torsion testing of rolled homogeneous armour. *Journal of Strain Analysis for Engineering Design*, 36:197–210, 2001.
- [7] B.B. Singh, G. Sukumar, A. Paman, G. Balaji, K.S. Kumar, V. Madhu, and R.A. Kumar. A comparative study on the ballistic performance and failure mechanisms of high-nitrogen steel and RHA steel against tungsten heavy alloy penetrators. *Journal of Dynamic Behavior of Materials*, 7:60–80, 2021.
- [8] J.D. Clayton. Analysis of shear localization in viscoplastic solids with pressure-sensitive structural transformations. *Journal of the Mechanics and Physics of Solids*, 193:105880, 2024.
- [9] M.R. Staker. The relation between adiabatic shear and material properties. *Acta Metallurgica*, 29:683–689, 1981.
- [10] Y.L. Bai. Thermo-plastic instability in simple shear. *Journal of the Mechanics and Physics of Solids*, 30:195–207, 1982.
- [11] A. Molinari and R.J. Clifton. Analytical characterization of shear localization in thermoviscoplastic materials. Technical Report DAAG29-85-K-0003/4, Brown University, Providence (RI), 1986.
- [12] A. Molinari and R.J. Clifton. Analytical characterization of shear localization in thermoviscoplastic materials. *ASME Journal of Applied Mechanics*, 54:806–812, 1987.
- [13] C. Fressengeas and A. Molinari. Instability and localization of plastic flow in shear at high strain rates. *Journal of the Mechanics and Physics of Solids*, 35:185–211, 1987.
- [14] A. Molinari. Shear band analysis. *Solid State Phenomena*, 3–4:447–467, 1988.
- [15] T.W. Wright. Approximate analysis for the formation of adiabatic shear bands. *Journal of the Mechanics and Physics of Solids*, 38:515–530, 1990.
- [16] D.E. Grady. Dynamics of adiabatic shear. *Journal de Physique IV*, 1:653–660, 1991.

- [17] B. Gurrutxaga-Lerma. Adiabatic shear banding and the micromechanics of plastic flow in metals. *International Journal of Solids and Structures*, 132:153–170, 2018.
- [18] T.G. Shawki, R.J. Clifton, and G. Majda. Analysis of shear band formation at high strain rates and the viscoplastic response of polycrystals. Technical Report DAAG-29-81-K-0121/3, Brown University, Providence (RI), 1983.
- [19] T.W. Wright and R.C. Batra. On stress collapse in adiabatic shear bands. *International Journal of Plasticity*, 1: 205–212, 1985.
- [20] T.W. Wright and J.W. Walter. On stress collapse in adiabatic shear bands. *Journal of the Mechanics and Physics of Solids*, 35:701–720, 1987.
- [21] H.P. Cherukuri and T.G. Shawki. An energy-based localization theory: I. Basic framework. *International Journal of Plasticity*, 11:15–40, 1995.
- [22] S.E. Schoenfeld and T.W. Wright. A failure criterion based on material instability. *International Journal of Solids and Structures*, 40:3021–3037, 2003.
- [23] R.C. Batra and B.M. Love. Adiabatic shear bands in functionally graded materials. *Journal of Thermal Stresses*, 27:1101–1123, 2004.
- [24] M. Fermen-Coker. Implementation of Schoenfeld-Wright failure criterion into a three-dimensional adiabatic shear band model in CTH. Technical Report ARL-TR-3284, Army Research Laboratory, Aberdeen Proving Ground (MD), 2004.
- [25] M. Zhou, A.J. Rosakis, and G. Ravichandran. On the growth of shear bands and failure-mode transition in prenotched plates: a comparison of singly and doubly notched specimens. *International Journal of Plasticity*, 14:435–451, 1998.
- [26] P. Longere, A. Dragon, H. Trumel, T. De Resseguier, X. Deprince, and E. Petitpas. Modelling adiabatic shear banding via damage mechanics approach. *Archive of Mechanics*, 55:3–38, 2003.
- [27] M. Dolinski and D. Rittel. Experiments and modeling of ballistic penetration using an energy failure criterion. *Journal of the Mechanics and Physics of Solids*, 83:1–18, 2015.
- [28] M. Dolinski, M. Merzer, and D. Rittel. Analytical formulation of a criterion for adiabatic shear failure. *International Journal of Impact Engineering*, 85:20–26, 2015.
- [29] C. McAuliffe and H. Waisman. A unified model for metal failure capturing shear banding and fracture. *International Journal of Plasticity*, 65:131–151, 2015.
- [30] C. McAuliffe and H. Waisman. A coupled phase field shear band model for ductile-brittle transition in notched plate impacts. *Computer Methods in Applied Mechanics and Engineering*, 305:173–195, 2016.
- [31] M. Arriaga and H. Waisman. Combined stability analysis of phase-field dynamic fracture and shear band localization. *International Journal of Plasticity*, 96:81–119, 2017.
- [32] Y. Xu, P. Ming, and J. Chen. A phase field framework for dynamic adiabatic shear banding. *Journal of the Mechanics and Physics of Solids*, 135:103810, 2020.
- [33] T. Wang, Z.L. Liu, Y.N. Cui, X. Ye, X.M. Liu, R. Tian, and Z. Zhuang. A thermo-elastic-plastic phase-field model for simulating the evolution and transition of adiabatic shear band. Part I. Theory and model calibration. *Engineering Fracture Mechanics*, 232:107028, 2020.
- [34] C. Samaniego, J. Ulloa, P. Rodriguez, G. Houzeaux, M. Vazquez, and E. Samaniego. A phase-field model for ductile fracture with shear bands: a parallel implementation. *International Journal of Mechanical Sciences*, 200:106424, 2021.
- [35] Q. Zeng, T. Wang, S. Zhu, H. Chen, and D. Fang. A rate-dependent phase-field model for dynamic shear band formation in strength-like and toughness-like modes. *Journal of the Mechanics and Physics of Solids*, 164: 104914, 2022.
- [36] V.I. Levitas, E. Stein, and M. Lengnick. On a unified approach to the description of phase transitions and strain localization. *Archive of Applied Mechanics*, 66:242–254, 1996.
- [37] A. Karma, D.A. Kessler, and H. Levine. Phase-field model of mode III dynamic fracture. *Physical Review Letters*, 87:045501, 2001.
- [38] V.I. Levitas, V.A. Levin, K.M. Zingerman, and E.I. Freiman. Displacive phase transitions at large strains: phase-field theory and simulations. *Physical Review Letters*, 103:025702, 2009.

- [39] J.D. Clayton and J. Knap. A phase field model of deformation twinning: nonlinear theory and numerical simulations. *Physica D*, 240:841–858, 2011.
- [40] V.I. Levitas, A.V. Idesman, and A.K. Palakala. Phase-field modeling of fracture in liquid. *Journal of Applied Physics*, 110:033531, 2011.
- [41] J.D. Clayton and J. Knap. A geometrically nonlinear phase field theory of brittle fracture. *International Journal of Fracture*, 189:139–148, 2014.
- [42] J. Choo and W. Sun. Coupled phase-field and plasticity modeling of geological materials: from brittle fracture to ductile flow. *Computer Methods in Applied Mechanics and Engineering*, 330:1–32, 2018.
- [43] D. Rittel, Z.G. Wang, and M. Merzer. Adiabatic shear failure and dynamic stored energy of cold work. *Physical Review Letters*, 96:075502, 2006.
- [44] D. Rittel, P. Landau, and A. Venkert. Dynamic recrystallization as a potential cause for adiabatic shear failure. *Physical Review Letters*, 101:165501, 2008.
- [45] M. Dolinski, D. Rittel, and A. Dorogoy. Modeling adiabatic shear failure from energy considerations. *Journal of the Mechanics and Physics of Solids*, 58:1759–1775, 2010.
- [46] J.D. Clayton and J. Knap. Nonlinear phase field theory for fracture and twinning with analysis of simple shear. *Philosophical Magazine*, 95:2661–2696, 2015.
- [47] Y. Me-Bar and D. Shechtman. On the adiabatic shear of Ti-6Al-4V ballistic targets. *Materials Science and Engineering*, 58:181–188, 1983.
- [48] Y. Xu, J. Zhang, Y. Bai, and M.A. Meyers. Shear localization in dynamic deformation: microstructural evolution. *Metallurgical and Material Transactions A*, 39:811–843, 2008.
- [49] P. Wang and K.S. Kumar. Dynamic deformation response of a high-strength, high-toughness Fe-10Ni-0.1C steel. *Materials Science and Engineering A*, 519:184–197, 2009.
- [50] N. Li, Y.D. Wang, R.L. Peng, X. Sun, P.K. Liaw, G.L. Wu, L. Wang, and H.N. Cai. Localized amorphism after high-strain-rate deformation in TWIP steel. *Acta Materialia*, 59:6369–6377, 2011.
- [51] C. Healy, S. Koch, C. Siemers, D. Mukherji, and G.J. Ackland. Shear melting and high temperature embrittlement: theory and application to machining titanium. *Physical Review Letters*, 114:165501, 2015.
- [52] C.A. Bronkhorst, E.K. Cerreta, Q. Xue, P.J. Maudlin, T.A. Mason, and G.T. Gray. An experimental and numerical study of the localization behavior of tantalum and stainless steel. *International Journal of Plasticity*, 22:1304–1335, 2006.
- [53] V.I. Levitas and K. Samani. Coherent solid/liquid interface with stress relaxation in a phase-field approach to the melting/solidification transition. *Physical Review B*, 84:140103, 2011.
- [54] Y.S. Hwang and V.I. Levitas. Internal stress-induced melting below melting temperature at high-rate laser heating. *Applied Physics Letters*, 104:263106, 2016.
- [55] Y.S. Hwang and V.I. Levitas. Superheating and melting within aluminum core-oxide shell nanoparticles for a broad range of heating rates: multiphysics phase field modeling. *Physical Chemistry Chemical Physics*, 18:28835–28853, 2016.
- [56] A.T. Goki and M. Javanbakht. Size-dependent melting of gold nanotube: phase field model and simulations and thermodynamic analytical solution. *Materials Today Communications*, 40:109641, 2024.
- [57] D. Sagapuram, K. Viswanathan, K.P. Trumble, and S. Chandrasekar. A common mechanism for evolution of single shear bands in large-strain deformation of metals. *Philosophical Magazine*, 98:3267–3299, 2018.
- [58] A. Marchand and J. Duffy. An experimental study of the formation process of adiabatic shear bands in a structural steel. *Journal of the Mechanics and Physics of Solids*, 36:251–283, 1988.
- [59] T.W. Wright. Toward a defect invariant basis for susceptibility to adiabatic shear bands. *Mechanics of Materials*, 17:215–222, 1994.
- [60] J.D. Clayton. Universal phase-field mixture representation of thermodynamics and shock wave mechanics in porous soft biologic continua. *Physical Review E*, 110:035001, 2024.
- [61] A. Morro. Wave propagation in thermo-viscous materials with hidden variables. *Archive of Mechanics*, 32:145–161, 1980.
- [62] A. Needleman. Material rate dependence and mesh sensitivity in localization problems. *Computer Methods in Applied Mechanics and Engineering*, 67:69–85, 1988.

- [63] J.D. Clayton. *Nonlinear Mechanics of Crystals*. Springer, Dordrecht, 2011.
- [64] J.D. Clayton and J.T. Lloyd. Finite strain continuum theory for phase transformations in ferromagnetic elastic-plastic solids. *Continuum Mechanics and Thermodynamics*, 34:1579–1620, 2022.
- [65] J.D. Clayton, H.A. Murdoch, J.T. Lloyd, D.J. Magagnosc, and D.M. Field. Modeling magnetic field and strain driven phase transitions and plasticity in ferrous metals. *Zeitschrift für Angewandte Mathematik und Mechanik (ZAMM)*, 104:e202200612, 2024.
- [66] J.D. Clayton. Nonlinear thermodynamic phase field theory with application to fracture and dynamic inelastic phenomena in ceramic polycrystals. *Journal of the Mechanics and Physics of Solids*, 157:104633, 2021.
- [67] V.I. Levitas. Thermomechanical theory of martensitic phase transformations in inelastic materials. *International Journal of Solids and Structures*, 35:889–940, 1998.
- [68] J.D. Clayton and D.L. McDowell. A multiscale multiplicative decomposition for elastoplasticity of polycrystals. *International Journal of Plasticity*, 19:1401–1444, 2003.
- [69] J.D. Clayton. *Differential Geometry and Kinematics of Continua*. World Scientific, Singapore, 2014.
- [70] J.D. Clayton. Analysis of shock compression of strong single crystals with logarithmic thermoelastic-plastic theory. *International Journal of Engineering Science*, 79:1–20, 2014.
- [71] J.D. Clayton. *Nonlinear Elastic and Inelastic Models for Shock Compression of Crystalline Solids*. Springer, Cham, 2019.
- [72] M.E. Gurtin. Generalized Ginzburg-Landau and Cahn-Hilliard equations based on a microforce balance. *Physica D*, 92:178–192, 1996.
- [73] K.C. Le, T.M. Tran, and J.S. Langer. Thermodynamic dislocation theory of adiabatic shear banding in steel. *Scripta Materialia*, 149:62–65, 2018.
- [74] J.D. Clayton. Dynamic plasticity and fracture in high density polycrystals: constitutive modeling and numerical simulation. *Journal of the Mechanics and Physics of Solids*, 53:261–301, 2005.
- [75] C.K.C. Lieou and C.A. Bronkhorst. Thermomechanical conversion in metals: dislocation plasticity model evaluation of the Taylor-Quinney coefficient. *Acta Materialia*, 202:170–180, 2021.
- [76] D.J. Bammann and G.C. Johnson. On the kinematics of finite-deformation plasticity. *Acta Mechanica*, 70:1–13, 1987.
- [77] U.F. Kocks, A.S. Argon, and M.F. Ashby. Thermodynamics and kinetics of slip. *Progress in Materials Science*, 19:1–291, 1975.
- [78] J.D. Clayton and A. Tonge. A nonlinear anisotropic elastic-inelastic constitutive model for polycrystalline ceramics and minerals with application to boron carbide. *International Journal of Solids and Structures*, 64–65:191–207, 2015.
- [79] A.R. Vishnu, J.C. Nieto-Fuentes, and J.A. Rodriguez-Martinez. Shear band formation in porous thin-walled tubes subjected to dynamic torsion. *International Journal of Solids and Structures*, 252:111837, 2022.
- [80] J.D. Clayton. Modeling dynamic plasticity and spall fracture in high density polycrystalline alloys. *International Journal of Solids and Structures*, 42:4613–4640, 2005.
- [81] C. Miehe, L.-M. Schaenzel, and H. Ulmer. Phase field modeling of fracture in multi-physics problems. Part I. Balance of crack surface and failure criteria for brittle crack propagation in thermo-elastic solids. *Computer Methods in Applied Mechanics and Engineering*, 294:449–485, 2015.
- [82] J.D. Clayton, R.B. Leavy, and J. Knap. Phase field modeling of heterogeneous microcrystalline ceramics. *International Journal of Solids and Structures*, 166:183–196, 2019.
- [83] C. Miehe, M. Hofacker, L.M. Schanzel, and F. Aldakheel. Phase field modeling of fracture in multi-physics problems. Part II. Coupled brittle-to-ductile failure criteria and crack propagation in thermo-elastic-plastic solids. *Computer Methods in Applied Mechanics and Engineering*, 294:486–522, 2015.
- [84] S. Na and W. Sun. Computational thermomechanics of crystalline rock, part I: a combined multi-phase-field/crystal plasticity approach for single crystal simulations. *Computer Methods in Applied Mechanics and Engineering*, 338:657–691, 2018.
- [85] M.J. Borden, T.J.R. Hughes, C.M. Landis, A. Anvari, and I.J. Lee. A phase-field formulation for fracture in ductile materials: finite deformation balance law derivation, plastic degradation, and stress triaxiality effects. *Computer Methods in Applied Mechanics and Engineering*, 312:130–166, 2016.

- [86] J.C. Boettger and D.C. Wallace. Metastability and dynamics of the shock-induced phase transition in iron. *Physical Review B*, 55:2840–2849, 1997.
- [87] J.D. Clayton and D.L. McDowell. Finite polycrystalline elastoplasticity and damage: multiscale kinematics. *International Journal of Solids and Structures*, 40:5669–5688, 2003.
- [88] J.D. Clayton and D.L. McDowell. Homogenized finite elastoplasticity and damage: theory and computations. *Mechanics of Materials*, 36:799–824, 2004.
- [89] R.F. Benck. Quasi-static tensile stress strain curves II. Rolled homogeneous armor. Technical Report BRL-MR-2703, US Army Ballistic Research Laboratory, Aberdeen Proving Ground (MD), 1976.
- [90] G.E. Hauver. The alpha-phase Hugoniot of rolled homogeneous armor. Technical Report BRL-MR-2651, US Army Ballistic Research Laboratory, Aberdeen Proving Ground (MD), 1976.
- [91] G.E. Hauver and A. Melani. The epsilon-phase Hugoniot of rolled homogeneous armor. Technical Report BRL-MR-2909, US Army Ballistic Research Laboratory, Aberdeen Proving Ground (MD), 1979.
- [92] G.L. Moss. Shear strains, strain rates and temperature changes in adiabatic shear bands. In M.A. Meyers and L.E. Murr, editors, *Shock Waves and High-strain-rate Phenomena in Metals: Concepts and Applications*, pages 299–312. Springer, Boston (MA), 1981.
- [93] G.T. Gray, S.R. Chen, W. Wright, and M.F. Lopez. Constitutive equations for annealed metals under compression at high strain rates and high temperatures. Technical Report LA-12669-MS, Los Alamos National Laboratory, Los Alamos (NM), 1994.
- [94] H.W. Meyer and D.S. Kleponis. An analysis of parameters for the Johnson-Cook strength model for 2-in-thick rolled homogeneous armor. Technical Report ARL-TR-2528, Army Research Laboratory, Aberdeen Proving Ground (MD), 2001.
- [95] J.D. Clayton and J.T. Lloyd. A dynamic finite-deformation constitutive model for steels undergoing slip, twinning, and phase changes. *Journal of Dynamic Behavior of Materials*, 7:217–247, 2021.
- [96] A. Sadjadpour, D. Rittel, G. Ravichandran, and K. Bhattacharya. A model coupling plasticity and phase transformation with application to dynamic shear deformation of iron. *Mechanics of Materials*, 80:255–263, 2015.
- [97] D. Rittel, G. Ravichandran, and A. Venkert. The mechanical response of pure iron at high strain rates under dominant shear. *Materials Science and Engineering A*, 432:191–201, 2006.
- [98] C.K. Syn, D.R. Lesuer, and O.D. Sherby. Microstructure in adiabatic shear bands in a pearlitic ultrahigh carbon steel. *Materials Science and Technology*, 21:317–324, 2005.
- [99] W. Wang, H. Zhang, M. Yang, P. Jiang, F. Yuan, and X. Wu. Shock and spall behaviors of a high specific strength steel: Effects of impact stress and microstructure. *Journal of Applied Physics*, 121:135901, 2017.
- [100] A.B. Belononshko, R. Ahuja, and B. Johansson. Quasi-ab initio molecular dynamic study of Fe melting. *Physical Review Letters*, 84:3638–3641, 2000.
- [101] J.H. Nguyen and N.C. Holmes. Melting of iron at the physical conditions of the earth’s core. *Nature*, 427:339–342, 2004.
- [102] M. Grinfeld. *Thermodynamic Methods in the Theory of Heterogeneous Systems*. Longman Scientific and Technical, Sussex, 1991.
- [103] H. Tan and T.J. Ahrens. Shock temperature measurements for metals. *High Pressure Research*, 2:159–182, 1990.
- [104] G.T. Gray. Classic split-Hopkinson bar testing. In H. Kuhn and D. Medlin, editors, *ASM Handbook*, volume 8, pages 462–476. ASM International, Materials Park, OH (USA), 2000.
- [105] L. Anand, K.H. Kim, and T.G. Shawki. Onset of shear localization in viscoplastic solids. *Journal of the Mechanics and Physics of Solids*, 35:407–429, 1987.
- [106] T.G. Shawki. Necessary and sufficient conditions for the onset of shear strain localization in thermal viscoplastic materials. Technical Report TAM-R-489, University of Illinois, Urbana (IL), 1988.